Progress In Electromagnetics Research, PIER 11, 1–49, 1995

FINITE-DIFFERENCE BEAM PROPAGATION METHOD FOR GUIDE-WAVE OPTICS

C. L. Xu and W. P. Huang

1. Introduction

Beam propagation method (BPM) is one of the most commonly used numerical methods for analysis and simulation of guided-wave propagation in inhomogeneous media. It was first introduced into fiber

optics by Feit and Fleck in 1978 to calculate the mode properties of optical fibers [1–3]. Since then many other waveguiding structures such as tapers and Y-junctions [4,5], bends [6], gratings [7], waveguide crossings [8], electrooptic waveguide modulators [9], fiber couplers [10,11] and nonlinear directional couplers [12] have been modeled and analyzed by the BPM.

The basic idea of the conventional BPM is to represent the electromagnetic field by a superposition of plane waves propagating in homogeneous media. The wave propagation in inhomogeneous media is modeled as an integral of these plane waves in the spectral domain and the effect of the inhomogeneity of the media is accounted for as a phase correction in the spatial domain at each propagation step. The FFT is used to provide the link between the spatial and the spectral domains, hence the method is named split-operator FFT-BPM. It can be expressed mathematically as:

$$\Psi(x, y, z + \Delta z) = PQP\Psi(x, y, z) \tag{1}$$

where $\Psi(x, y, z)$ and $\Psi(x, y, z + \Delta z)$ are field distributions at two subsequent propagation steps, P is a propagator which can be solved by the FFT, and Q is a phase correction.

The distinct advantages of the BPM are that (1) it applies to a structure with an arbitrary cross-section; (2) both the guided and the radiative waves are included in the analysis. As long as the input field is given, the BPM is capable of tracing the wave propagation in the given structure. However, there are some limitations in the conventional FFT-BPM.

1. The formulation of the FFT-BPM is derived under the assumption that the refractive index difference in the transverse direction is very small so that the phase error term can be expressed by the first-order term in a Taylor series. Therefore, the FFT-BPM can not be applied to structures with large index discontinuities.
2. The use of the FFT in the conventional BPM leads to a computation efficiency that is of the order $N \log N$. Furthermore, the number of mesh points N must be a integer power of 2. Additionally, the mesh size has to be uniform. Consequently, for complex structures, the FFT-BPM becomes less efficient.
3. A paraxial approximation has been made in the derivation, therefore the FFT-BPM is accurate only when the beam propagates in the direction with a small angle to the z-axis.

4. The FFT-BPM can only trace the scalar wave propagation, hence the vectorial properties, such as the polarization dependence and polarization coupling of the guided-wave devices can not be described.

Some effort has been made to adapt the BPM to treat strongly guided waveguides [13–16]. For instance, the split-step finite-difference BPM developed by Yevick and Hermanson was used to simulate strongly guiding semiconductor-based rib waveguides [17,18]. Instead of using the FFT, the split-step FD-BPM solves the propagator in (1) by the finite-difference method. The conventional phase correction is still retained in the algorithm.

To improve the efficiency and the flexibility, a finite-difference beam propagation method (FD-BPM) was developed by Hendow and Shakir to solve the paraxial scalar wave equation directly by the finite-difference method [19]. The original application of the FD-BPM was limited to cylindrically symmetric structures. Chung and Dagli introduced the FD-BPM to the Cartesian coordinate system [20]. A comparison with the FFT-BPM [20,21] has been made and the conclusion is that the FD-BPM is more accurate and efficient than the FFT-BPM. The computation is proportional to the number of mesh points N, for a given cross-section, instead of $N \log N$ in FFT-BPM. Also, the number of mesh points N can be any number, not necessarily a integer power of 2 as required by the FFT-BPM. In addition, the introduction of a nonuniform and adaptive mesh into the FD-BPM could increase the efficiency significantly [22–26].

Recently, there has been a lot of effort on developing a vectorial BPM which can describe the propagation of vectorial electromagnetic waves and considerable progress has been made in the past three years. An implicit 2-D vectorial FD-BPM was first developed by Huang, Xu, Chu, and Chaudhuri in 1991 [27,28]. It has been extended to 3-D semi-vectorial FD-BPM by Liu and Li [29,30]. Shortly after that, a full-vectorial FD-BPM has been developed by Huang, Xu, and Chaudhuri [31,32]. In the full-vectorial FD-BPM, both the polarization dependence and polarization coupling are taken into account. The full-vectorial BPM may be reduced to the semi-vectorial BPM if only the polarization dependence is considered and the polarization coupling is ignored. In addition, two explicit numerical algorithms for the FD-VBPM have been developed. One is based on multi-step discretization

by Chung, Dagli, and Thylen [33]; The other is based on series expansion by Bothe, Splett, Unlenderf and Pertermann [34]. Since then, some modifications have been made such as the wide-angle implicit scheme by Huang and Xu [36], and the wide-angle explicit scheme by Chung and Dagli [35].

In this chapter, a finite-difference vectorial beam propagation method (FD-VBPM) is described. Section 2 gives the detailed mathematical derivation of paraxial and wide-angle wave equations. In section 3, the FD-VBPM is analyzed using the von Neumann method. A thorough assessment is performed by comparing numerical results with the exact analytical solutions. In section 4, other finite-difference schemes are introduced and a comparison among different schemes is made. In the last section, the FD-VBPM is extended to anisotropic waveguides.

2. Mathematical Formulations

The electromagnetic wave propagation in an arbitrary medium can be described rigorously by Maxwell's equations and their associated constitutive relations as well as boundary conditions. However, a direct solution of Maxwell's equations is usually difficult and the exact analytical expressions for such a solution can be found only for a limited number of simple structures, such as step-index slab waveguides and step-index fibers. Numerical solutions may be possible for more complicated problems, which can not be solved analytically. To make the numerical solution feasible, certain assumptions have to be made to simplify Maxwell's equations for specific applications. In this section, a vectorial Helmholtz equation is first derived directly from Maxwell's equations. For different interests and applications, the Helmholtz equation can be reduced to different forms.

2.1 Vectorial Helmholtz Equations

Maxwell's equations in their general form are written as

$$\nabla \times \vec{\mathbf{E}} = -j\omega\mu_o\vec{\mathbf{H}} \tag{2}$$

$$\nabla \times \vec{\mathbf{H}} = j\omega n^2\epsilon_o\vec{\mathbf{E}} \tag{3}$$

for continuous waves in linear and isotropic media. By taking the curl of (2) and using (3), a vectorial wave equation can be derived:

$$\nabla \times \nabla \times \vec{\mathbf{E}} - n^2 k^2 \vec{\mathbf{E}} = 0 \tag{4}$$

By using the vector identity

$$\nabla \times \nabla \times = \nabla(\nabla \cdot) - \nabla^2 \tag{5}$$

Equation (4) becomes

$$\nabla^2 \vec{\mathbf{E}} + n^2 k^2 \vec{\mathbf{E}} = \nabla(\nabla \cdot \vec{\mathbf{E}}). \tag{6}$$

If the transverse components of an electromagnetic field are known, then the longitudinal component may be readily obtained by application of the zero divergence constraint $\nabla \cdot (n^2 \vec{\mathbf{E}}) = 0$. Therefore, the transverse components are sufficient to describe the vectorial properties of the electromagnetic field. The transverse component of (6) is:

$$\nabla^2 \vec{\mathbf{E}}_t + n^2 k^2 \vec{\mathbf{E}}_t = \nabla_t \left(\nabla_t \cdot \vec{\mathbf{E}}_t + \frac{\partial E_z}{\partial z} \right) \tag{7}$$

where the subscript "t" stands for the transverse components.

Using Gauss' law,

$$\nabla \cdot (n^2 \vec{\mathbf{E}}_t) = 0 \tag{8}$$

we obtain:

$$\nabla_t \cdot (n^2 \vec{\mathbf{E}}_t) + \frac{\partial n^2}{\partial z} E_z + n^2 \frac{\partial E_z}{\partial z} = 0. \tag{9}$$

If the refractive index $n(x, y, z)$ varies slowly along the propagation direction z, which is valid for most photonic guided-wave devices, then $\frac{\partial n^2}{\partial z} E_z$ is much smaller than the other two terms in (9). Thus one can derive

$$\frac{\partial E_z}{\partial z} \approx -\frac{1}{n^2} \nabla_t \cdot (n^2 \vec{\mathbf{E}}_t). \tag{10}$$

The above equation is exact for z-invariant structures where $\frac{\partial n^2}{\partial z} = 0$.

By substituting (10) into (7), one obtains a vectorial Helmholtz equation based on the transverse electric fields

$$\nabla^2 \vec{\mathbf{E}}_t + n^2 k^2 \vec{\mathbf{E}}_t = \nabla_t \left[\nabla_t \cdot \vec{\mathbf{E}}_t - \frac{1}{n^2} \nabla_t \cdot (n^2 \vec{\mathbf{E}}_t) \right]. \tag{11}$$

The term on the RHS contains the vectorial properties of the electromagnetic field.

Following the same procedure, one can derive a vectorial Helmholtz equation based on the transverse magnetic fields

$$\nabla^2\vec{\mathbf{H}}_t + n^2k^2\vec{\mathbf{H}}_t = -\frac{1}{n^2}\nabla_t n^2 \times (\nabla_t \times \vec{\mathbf{H}}_t) \tag{12}$$

The vectorial Helmholtz equations may degenerate into different variants under certain assumptions and approximation.

2.2 One-Way Wave Equations

By assuming the wave travels along $+z$ direction, the field can be separated as a slowly-varying envelope and a fast-oscillating phase term

$$\vec{\mathbf{E}}_t(x,y,z) = \mathbf{E}_t(x,y,z)e^{-jn_o kz} \tag{13}$$

where n_o is a reference index. n_o should be chosen close to the effective index such that the envelope varies slowly. By substituting (13) into (11), one is able to derive the one-way wave equation based on the transverse electric fields,

$$\frac{\partial}{\partial z}\left(j2n_o k - \frac{\partial}{\partial z}\right)\mathbf{E}_t = \mathbf{P}\mathbf{E}_t \tag{14}$$

where the operator $\mathbf{P}$ is defined by

$$\mathbf{P}\mathbf{E}_t = \nabla_t^2\mathbf{E}_t + (n^2 - n_o^2)k^2\mathbf{E}_t - \nabla_t\left[\nabla_t \cdot \mathbf{E}_t - \frac{1}{n^2}\nabla_t \cdot (n^2\mathbf{E}_t)\right]. \tag{15}$$

Or written in components [28,32]

$$P_{xx}E_x = \frac{\partial}{\partial x}\left[\frac{1}{n^2}\frac{\partial(n^2E_x)}{\partial x}\right] + \frac{\partial^2 E_x}{\partial y^2} + k^2(n^2 - n_o^2)E_x \tag{16}$$

$$P_{yy}E_y = \frac{\partial^2 E_y}{\partial x^2} + \frac{\partial}{\partial y}\left[\frac{1}{n^2}\frac{\partial(n^2E_y)}{\partial y}\right] + k^2(n^2 - n_o^2)E_y \tag{17}$$

$$P_{xy}E_y = \frac{\partial}{\partial x}\left[\frac{1}{n^2}\frac{\partial(n^2E_y)}{\partial y}\right] - \frac{\partial^2 E_y}{\partial x \partial y} \tag{18}$$

$$P_{yx}E_x = \frac{\partial}{\partial y}\left[\frac{1}{n^2}\frac{\partial(n^2E_x)}{\partial x}\right] - \frac{\partial^2 E_x}{\partial y \partial x}. \tag{19}$$

It is noted that Eqs. (16)–(19) are arranged in such a convenient fashion that all the differentiated terms are continuous. Thus, they can be ready discretized without any extra special treatment.

Similarly, one is able to derive the one-way wave equation based on the transverse magnetic fields.

$$\frac{\partial}{\partial z}\left(j2n_o k - \frac{\partial}{\partial z}\right)\mathbf{H_t} = \mathbf{Q}\mathbf{H_t} \tag{20}$$

where the operator

$$\mathbf{Q} = \begin{pmatrix} Q_{xx} & Q_{xy} \\ Q_{yx} & Q_{yy} \end{pmatrix} \tag{21}$$

is defined as [31]

$$Q_{xx}H_x = \frac{\partial^2 H_x}{\partial x^2} + n^2\frac{\partial}{\partial y}\left(\frac{1}{n^2}\frac{\partial H_x}{\partial y}\right) + (n^2 - n_o^2)k^2E_x \tag{22}$$

$$Q_{yy}H_y = \frac{\partial^2 H_y}{\partial y^2} + n^2\frac{\partial}{\partial x}\left(\frac{1}{n^2}\frac{\partial H_y}{\partial x}\right) + (n^2 - n_o^2)k^2H_y \tag{23}$$

$$Q_{xy}H_y = \frac{\partial^2 H_y}{\partial y \partial x} - n^2\frac{\partial}{\partial y}\left(\frac{1}{n^2}\frac{\partial H_y}{\partial x}\right) \tag{24}$$

$$Q_{yx}H_x = \frac{\partial^2 H_x}{\partial x \partial y} - n^2\frac{\partial}{\partial x}\left(\frac{1}{n^2}\frac{\partial H_x}{\partial y}\right). \tag{25}$$

Like the operator $\mathbf{P}$, every term in Eqs. [22–25] is continuous and can be discretized directly.

2.3 Paraxial and Wide-Angle Wave Equations

The one-way wave equations can be reduced to paraxial and wide-angle wave equations by applying the Pade approximation

$$\left.\frac{\partial}{\partial z}\right|_{i+1} = \frac{\mathbf{P}}{j2n_o k - \frac{\partial}{\partial z}|_i} \tag{26}$$

with $\frac{\partial}{\partial z}|_0 = 0$. By letting $i = 1$, one can derive the paraxial wave equation

$$j2n_o k\frac{\partial \mathbf{E_t}}{\partial z} = \mathbf{P}\mathbf{E_t}. \tag{27}$$

The first-order wide-angle wave equation

$$j\left(2n_o k + \frac{\mathbf{P}}{2n_o k}\right)\frac{\partial \mathbf{E_t}}{\partial z} = \mathbf{P}\mathbf{E_t} \tag{28}$$

can be derived by letting $i = 2$. In principle, the wide angle formulation can be carried out to any higher order as demonstrated in Ref. [39].

It is straightforward to obtain the similar equations for the transverse magnetic fields simply by replacing $\mathbf{P}$ and $\mathbf{E}$ by $\mathbf{Q}$ and $\mathbf{H}$.

2.4 Semi-Vectorial and Scalar Wave Equations

Equations (27)–(28) are full-vectorial wave equations. The vectorial properties of the electromagnetic fields are included. $P_{xx} \neq P_{yy}$ causes the polarization dependence. $P_{xy} \neq 0$ and $P_{yx} \neq 0$ leads to the hybrid nature (i.e. the polarization mixing). The discontinuities of the normal component of electric field at index interfaces, which is responsible for the vectorial properties, have been considered in the formulations.

If the coupling between the two polarizations is weak and negligible, which is true for most optical guided-wave devices, a semi-vectorial treatment is sufficient. By neglecting the cross-coupling terms P_{xy} and P_{yx}, the full-vectorial paraxial Eq. (27) as well as the wide-angle Eq. (28) reduce to two pair of decoupled semi-vectorial equations:

$$j2n_o k\frac{\partial E_x}{\partial z} = P_{xx}E_x \tag{29}$$

$$j\left(2n_o k + \frac{P_{xx}}{2n_o k}\right)\frac{\partial E_x}{\partial z} = P_{xx}E_x; \tag{30}$$

for E_x, and

$$j2n_o k\frac{\partial E_y}{\partial z} = P_{yy}E_y \tag{31}$$

$$j\left(2n_o k + \frac{P_{yy}}{2n_o k}\right)\frac{\partial E_y}{\partial z} = P_{yy}E_y. \tag{32}$$

for E_y.

As we have mentioned, the equations for the transverse magnetic fields can be obtained simply by replacing P_{xx}, P_{yy}, E_x, and E_y by Q_{xx}, Q_{yy}, H_x, and H_y, respectively.

If the structures are weakly-guiding, even the polarization dependence caused by geometry may be neglected and the following scalar approximation can be made

$$P = P_{xx} = P_{yy} = Q_{xx} = Q_{yy} = \frac{\partial^2}{\partial x^2} + \frac{\partial^2}{\partial y^2} + k^2(n^2 - n_o^2) \tag{33}$$

and the semi-vectorial equations for both electric and magnetic fields can be replaced by one single scalar wave equation,

$$j2n_o k\frac{\partial \Psi}{\partial z} = P\Psi \tag{34}$$

for the paraxial equation, and

$$j\left(2n_o k + \frac{P}{2n_o k}\right)\frac{\partial \Psi}{\partial z} = P\Psi \tag{35}$$

for the wide-angle equation. Here both Ψ and its derivatives are assumed to be continuous everywhere.

2.5 Finite-Difference Discretizations

As described, all terms in Eqs. (16)–(19) are continuous and can be discretized directly. Let $E_x(i,j)$, $E_y(i,j)$ and $n_{i,j}$ represent the electric fields and the refractive index at the mesh (i,j) with mesh size Δx and Δy. The finite difference expressions of Eqs. (16)–(19) are:

$$P_{xx}E_x = \frac{T^x_{i+1,j}E_x(i+1,j) - T^x_{i,j}E_x(i,j) + T^x_{i-1,j}E_x(i-1,j)}{(\Delta x)^2}$$

$$\frac{E_x(i,j+1) - 2E_x(i,j) + E_x(i,j-1)}{(\Delta y)^2} + (n^2_{i,j} - n_o^2)k^2E_x(i,j) \tag{36}$$

where

$$T^x_{i\pm1,j} = \frac{n^2_{i\pm1,j} + n^2_{i,j}}{2n^2_{i,j}}$$

$$T^x_{i,j} = \frac{n^2_{i-1,j} + n^2_{i,j}}{2n^2_{i-1,j}} + \frac{n^2_{i+1,j} + n^2_{i,j}}{2n^2_{i+1,j}}$$

and

$$\begin{aligned} P_{yy}E_y =& \frac{T^y_{i,j+1}E_y(i,j+1) - T^y_{i,j}E_y(i,j) + T^y_{i,j-1}E_y(i,j-1)}{(\Delta y)^2} \\ &+ \frac{E_y(i+1,j) - 2E_y(i,j) + E_y(i-1,j)}{(\Delta x)^2} \\ &+ (n^2_{i,j} - n^2_o)k^2E_y(i,j) \end{aligned} \tag{37}$$

where

$$T^y_{i,j\pm1} = \frac{n^2_{i,j\pm1} + n^2_{i,j}}{2n^2_{i,j}}$$

$$T^y_{i,j} = \frac{n^2_{i,j-1} + n^2_{i,j}}{2n^2_{i,j-1}} + \frac{n^2_{i,j+1} + n^2_{i,j}}{2n^2_{i,j+1}}$$

Similarly, P_{xy} and P_{yx} are expressed by

$$\begin{aligned} P_{xy}E_y = \frac{1}{4\Delta x\Delta y}\Bigg\{ & \left[\frac{n^2_{i+1,j+1}}{n^2_{i+1,j}} - 1\right] E_y(i+1,j+1) \\ & - \left[\frac{n^2_{i+1,j-1}}{n^2_{i+1,j}} - 1\right] E_y(i+1,j-1) \\ & - \left[\frac{n^2_{i-1,j+1}}{n^2_{i-1,j}} - 1\right] E_y(i-1,j+1) \\ & + \left[\frac{n^2_{i-1,j-1}}{n^2_{i-1,j}} - 1\right] E_y(i-1,j-1)\Bigg\} \end{aligned} \tag{38}$$

$$P_{yx}E_x = \frac{1}{4\Delta y\Delta x}\left\{\left[\frac{n^2_{i+1,j+1}}{n^2_{i,j+1}} - 1\right]E_x(i+1,j+1)\right.$$
$$-\left[\frac{n^2_{i-1,j+1}}{n^2_{i,j+1}} - 1\right]E_x(i-1,j+1)$$
$$-\left[\frac{n^2_{i+1,j-1}}{n^2_{i,j-1}} - 1\right]E_x(i+1,j-1)$$
$$\left.+\left[\frac{n^2_{i-1,j-1}}{n^2_{i,j-1}} - 1\right]E_x(i-1,j-1)\right\}. \tag{39}$$

Eqs. (22)–(25) for the transverse magnetic field can also be discretized directly and the finite difference expressions are:

$$Q_{xx}H_x$$
$$=\frac{R_{i,j+1}H_x(i,j+1) - [R_{i,j+1}+R_{i,j-1}]H_x(i,j) + R_{i,j-1}H_x(i,j-1)}{(\Delta y)^2}$$
$$+\frac{H_x(i+1,j) - 2H_x(i,j) + H_x(i-1,j)}{(\Delta x)^2} + (n^2_{i,j} - n^2_o)k^2H_x(i,j) \tag{40}$$

$$Q_{yy}H_y$$
$$=\frac{R_{i+1,j}H_y(i+1,j) - (R_{i+1,j}+R_{i-1,j})H_y(i,j) + R_{i-1,j}H_y(i-1,j)}{(\Delta x)^2}$$
$$+\frac{H_y(i,j+1) - 2H_y(i,j) + H_y(i,j-1)}{(\Delta y)^2} + (n^2_{i,j} - n^2_o)k^2H_y(i,j) \tag{41}$$

where

$$R_{i,j\pm1} = \frac{n^2_{i,j\pm1} + n^2_{i,j}}{2n^2_{i,j\pm1}}$$

and

$$R_{i\pm1,j} = \frac{n_{i\pm1,j}^2 + n_{i,j}^2}{2n_{i\pm1,j}^2}$$

Similarly, Q_{xy} and Q_{yx} are expressed by

$$\begin{aligned} Q_{xy}H_y = \frac{1}{4\Delta x\Delta y}\Bigg\{ & \left[1 - \frac{n_{i,j}^2}{n_{i,j+1}^2}\right] H_y(i+1,j+1) \\ & - \left[1 - \frac{n_{i,j}^2}{n_{i,j-1}^2}\right] H_y(i+1,j-1) \\ & - \left[1 - \frac{n_{i,j}^2}{n_{i,j+1}^2}\right] H_y(i-1,j+1) \\ & + \left[1 - \frac{n_{i,j}^2}{n_{i,j-1}^2}\right] H_y(i-1,j-1)\Bigg\} \end{aligned} \tag{42}$$

$$\begin{aligned} Q_{yx}H_x = \frac{1}{4\Delta y\Delta x}\Bigg\{ & \left[1 - \frac{n_{i,j}^2}{n_{i+1,j}^2}\right] H_x(i+1,j+1) \\ & - \left[1 - \frac{n_{i,j}^2}{n_{i-1,j}^2}\right] H_x(i-1,j+1) \\ & - \left[1 - \frac{n_{i,j}^2}{n_{i+1,j}^2}\right] H_x(i+1,j-1) \\ & + \left[1 - \frac{n_{i,j}^2}{n_{i-1,j}^2}\right] H_x(i-1,j-1)\Bigg\} \end{aligned} \tag{43}$$

3. Finite-Difference Beam Propagation Method

In this section, we will describe how to develop a finite-difference beam propagation method (FD-BPM) by solving the wave equations derived in the previous section, as well as how to implement the numerical boundary conditions. The FD-BPM is then analyzed by the von

Neumann method and key issues, such as stability, numerical dissipation, and numerical dispersion of the numerical scheme are addressed. Finally, the FD-BPM is validated by comparing it with exact analytical solutions for both 2-D and 3-D waveguides and the effects of the key parameters are assessed.

3.1 Numerical Scheme

As was mentioned in Section 2, the 3-D semi-vectorial and the 2-D formulations are the reduced forms of the full-vectorial equations under certain approximations. Therefore, conclusions drawn from the full-vectorial equations are expected to be valid for the semi-vectorial and the 2-D cases. For this reason, the analysis is carried out for the general full-vectorial case.

The solution to Eq. (27) can be written in an exponential form

$$\mathbf{E}_t(x, y, z + \Delta z) = e^{-j\mathbf{P}\Delta z}\mathbf{E}_t(x, y, z) \tag{44}$$

which can also be approximated by a weighted finite-difference form

$$\mathbf{E}_t(x, y, z + \Delta z) = \frac{2n_o k - j\Delta z(1-\alpha)\mathbf{P}}{2n_o k + j\Delta z\alpha\mathbf{P}}\mathbf{E}_t(x, y, z) \tag{45}$$

where Δz is the longitudinal step size and α is a weighting factor which controls the finite-difference scheme. For instance, $\alpha = 1$ corresponds to the standard implicit scheme and $\alpha = 0$ is explicit; the Crank-Nicholson scheme corresponds to $\alpha = 0.5$. The choice of α will affect the stability, the numerical dissipation, and the numerical dispersion of the scheme, which will be discussed later in Section 3.3.

By discretizing the operator $\mathbf{P}$ in Eq. (45) as described in the previous section, we obtain a system of linear equations

$$\mathbf{A}\,[\mathbf{E}_t]^{l+1} = \mathbf{B}\,[\mathbf{E}_t]^l \tag{46}$$

where $[\mathbf{E}_t]^l$ and $[\mathbf{E}_t]^{l+1}$ are field vectors at two sequential steps l and $l+1$, $\mathbf{A}$ and $\mathbf{B}$ are nonsymmetric complex band matrices. The matrix $\mathbf{A}$, which has nine non-zero elements in each row for the 3-D full-vectorial equations and five non-zero elements for the 3-D semi-vectorial and scalar equations, can be inverted efficiently by well-established sparse matrix solvers, such as ORTHOMIN [41], BiCG [42],

or BiCG-STAB [43]. For the 2-D structures, the matrix **A** reduces to a tri-diagonal matrix which can inverted directly by a **LU** solver [40].

3.2 Transparent Boundary Condition

The Maxwell's equations and their reduced forms can not be solved numerically without specifying the boundary conditions since the numerical computation window can not have an infinite dimension. The boundary condition used in the conventional BPM is the so-called absorbing boundary condition [13]. The idea is to artificially place a lossy medium at the edges of the computation window to absorb (or to eliminate) the possible reflections at the boundary. The major disadvantage of the absorbing boundary condition is that it is problem dependent. For a specific structure, users have to choose different absorbing parameters, such as the thickness of the lossy region and the magnitude of the artificial loss. All of these require experience and perhaps trial-and-error experiment. In addition, to minimize the artificial loss, the window size has to be large enough so that the fields at boundary are almost zero. A new boundary condition, called transparent boundary condition has been proposed lately [44]. The transparent boundary condition has distinguished advantages over the absorbing boundary condition. First, it is not problem dependent and much more robust. Therefore, the users do not need to deal with the numerical boundary conditions, which are automatically set in the numerical algorithm. Secondly, it does not require a zero value at the boundary. Hence, the wave can travel smoothly out of the computation window without reflection, leading to a relatively small computation window which can be used to increase the efficiency.

The wave equation at the computation edges is assumed to be a one-way plane wave which satisfies

$$\frac{\partial \Psi}{\partial x} = -jk_x \Psi. \tag{47}$$

In the finite-difference form, this becomes

$$\Psi^{l+1}(m) = \Psi^{l+1}(m-1)e^{-jk_x \Delta x} \tag{48}$$

where the transverse complex wave vector k_x is computed from the previous step by calculating the ratio $\Psi^l(m-1)/\Psi^l(m-2)$. To avoid possible reflection due to numerical errors, the real part of the transverse complex wave vector k_x is forced to be non-negative.

3.3 von Neumann Analysis

To analyze the FD-BPM, we apply the von Neumann method. Strictly speaking, the von Neumann method is valid only when the refractive index is independent of x, y, and z. If the refractive index is slowly varying in the region of interest or piecewise uniform, then the von Neumann analysis may be applied locally. It can be shown that advancing $\mathbf{E}_t$ in the spatial domain by one longitudinal step corresponds to multiplication by the amplification factor g, given by

$$g = \frac{2n_o k - j\Delta z(1-\alpha) \parallel \mathbf{P} \parallel}{2n_o k + j\Delta z \alpha \parallel \mathbf{P} \parallel} \tag{49}$$

where $\parallel \mathbf{P} \parallel$ is the norm of the operator $\mathbf{P}$ which is related to the wavelength, the transverse step sizes, as well as the index profile at the middle of two propagating steps.

The amplification factor g contains information about the stability, the numerical dissipation and dispersion of the finite-difference schemes and will be used in the analysis of the FD-BPM.

A. Stability criteria

The finite-difference scheme is stable if $|g| \leq 1$. From Eq. (49), it is readily proved that the weighted finite-difference scheme in Eq. (45) is unconditionally stable for

$$\alpha \geq 0.5, \tag{50}$$

which means that the stability criteria is independent of both longitudinal step size and transverse mesh sizes. The numerical boundary conditions used may also have effects on the stability of the schemes. Under these circumstances, the Crank-Nicolson scheme with $\alpha = 0.5$ is more likely to become unstable compared to the implicit scheme with $\alpha > 0.5$.

B. Numerical dissipation

A stable numerical scheme may not conserve power. The numerical dissipation may introduce nonphysical power loss and will limit the application of the FD-BPM for prediction of the guided power. Theoretically, a nondissipative finite-difference scheme requires $|g| = 1$,

which corresponds to the Crank-Nicolson scheme. Generally speaking, the Crank-Nicolson scheme is the least dissipative while the standard implicit scheme with $\alpha = 1$ is the most. In practice, α should be carefully chosen. Although the Crank-Nicolson scheme is theoretically stable and nondissipative, $\alpha = 0.5$ may not be the best choice since the numerical boundary condition may have some effects on the stability. Also, the inevitable high frequency numerical noise will keep propagating due to the nondissipative scheme. As a result, the simulated field patterns are usually not smooth due to the high frequency numerical noise. The suggested scheme should be $\alpha = 0.5 + \delta$ (δ is a very small number) such that the scheme is slightly dissipative in order to smooth the results but not to violate power conservation. On the other hand, even for a dissipative scheme, the numerical dissipation can always be reduced by reducing the longitudinal step size Δz, as evident from Eq. (49).

C. Numerical dispersion.

Due to the discretization, some phase errors will be introduced in a finite-difference scheme. As a result, the numerical dispersion will generate and degrade the accuracy of the phase-related characteristics calculated by using the FD-BPM, such as the propagation constants and coupling lengths of the optical waveguides. By assuming that the refractive index is slowly varying, we may still apply the von Neumann method to analyze the numerical dispersion. The solution to Eq. (45) may be rewritten as

$$\mathbf{E}_t{}^l(m,n) = |g^l| e^{-j(mk_x\Delta x + nk_y\Delta y + lk_z\Delta z)} \tag{51}$$

where $\mathbf{E}_t{}^l(m,n)$ is the field value at the lattice points of $x = m\Delta x$, $y = n\Delta y$, and $z = l\Delta z$. The propagation constant for the envelope of the transverse electric fields along z can be approximated by

$$k_z \approx \frac{1}{2kn_o}\left[(n^2 - n_o^2)k^2 - \frac{4}{(\Delta x)^2}\sin^2\left(\frac{k_x\Delta x}{2}\right) - \frac{4}{(\Delta y)^2}\sin^2\left(\frac{k_y\Delta y}{2}\right)\right] \tag{52}$$

Equation (52) indicates that the scheme parameter α and the longitudinal step size Δz do not affect the numerical dispersion. To reduce

the numerical dispersion, one needs to choose a proper reference index n_o and use a sufficiently fine mesh in the transverse cross section (i.e., to reduce Δx and Δy).

3.4 Assessment

For the assessment, we simulated the guided modes of a step-index symmetric slab waveguide and a step-index fiber, for which the exact analytical solutions are available for comparison. These simple structures lend themselves to easy understanding and interpretation of the results obtained from the numerical simulations.

A. 2-D slab waveguide

The numerical dissipation and the numerical dispersion are two key parameters to evaluate a numerical scheme. To assess the FD-BPM, we calculate the power attenuation coefficients along the waveguide axis and the percentage errors of the propagation constants of the TE and the TM guided-modes. According to our analysis in section 3.3, the power attenuation experienced by a guided mode in this lossless and uniform (or z-invariant) waveguide structure is nonphysical and mainly attributed to the numerical dissipation of the finite-difference schemes. The errors in the propagation constants are mainly due to the numerical dispersion as well as the truncation errors caused by the discretization.

At the input, we start with the electric fields of the guided modes calculated from the exact analytical solutions. The propagation constants of the guided-modes are computed by first propagating the fields a certain distance and then performing an overlap integral between the input and the propagating fields [28]. The propagation constants for the guided modes can be extracted from the overlap integrals. The power attenuation coefficients are evaluated by calculating the the total power along the propagation distance. The insertion loss due to the mismatch between the exact normal mode and the discretized waveguide structures has been considered. The refractive indices chosen for the guiding and the cladding layers are $n_1 = 1.5$, $n_2 = 1.3$, respectively. The total width of the guiding layer is $D = 0.5\mu m$. The wavelength is $\lambda = 1.5\mu m$.

We first evaluate the effect of the reference index n_o and the scheme parameter α. Shown in Figs. 1(a) and 1(b) are the percentage errors of the propagation constants and the power attenuation coefficients (dB/mm) for the TE (solid) and the TM (dash) modes for $\alpha = 0.5$ and $\alpha = 0.6$, respectively. The mesh size is $\Delta x = 0.02\mu m$ and the step size is $\Delta z = 0.01\mu m$. The effective indices n_{eff} of the TE and TM modes are calculated and marked in the figures. It is noted that the propagation constant is independent of α, but critically dependent on n_o. The best results are achieved when $n_o \approx n_{\text{eff}}$. All the observations are consistent with the analysis in section 3.3. It should be pointed out that the n_o dependence can be reduced significantly by using wide-angle BPM [36].

By inspecting the power attenuation show in Fig. 1(b), it is noted that the nondissipative Crank-Nicolson scheme with $\alpha = 0.5$ is power conserved and the power attenuation is independent of n_o. For the other schemes ($\alpha > 0.5$), the larger α is, the more dependent the numerical dissipation is on the reference index n_o. These results are also consistent with the analysis in section 3.3. Therefore, in the situation where the effective index n_{eff} is difficult to estimate, the Crank-Nicolson or schemes with α slightly larger than 0.5 are preferred for predicting the guided power in the waveguides.

With the proper choice of the reference index n_o and the scheme parameter α, we now proceed to investigate the convergence of the FD-BPM as functions of the mesh size. Figs. 2(a) and 2(b) show the percentage errors of the propagation constants and the attenuation coefficients for the TE (solid curves) and TM (dash curves) modes as function of the mesh size Δx. The longitudinal step size is fixed at $\Delta z = 0.01\mu m$. The scheme parameter is $\alpha = 0.6$. It is apparent from Fig. 2(a) that the propagation constants calculated by the FD-BPM converge to the exact solutions as $\Delta x \to 0$. This observation can be explained by the von Neumann analysis. By reducing the mesh size Δx, the numerical dispersion is reduced as indicated in Eq. (52), thereby leading to more accurate propagation constants. The influence of the mesh size on the power attenuation coefficients is small unless Δx is large, as illustrated in Fig. 2(b).

(a)

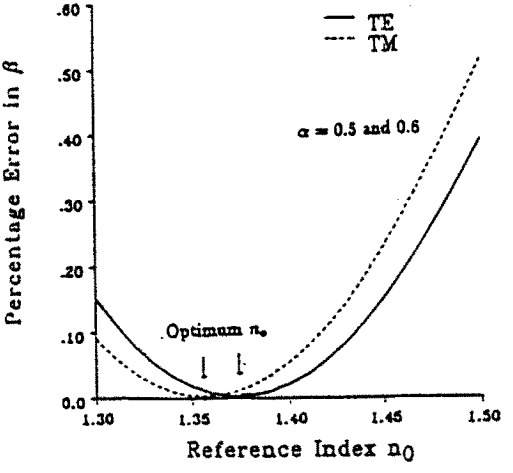

(b)

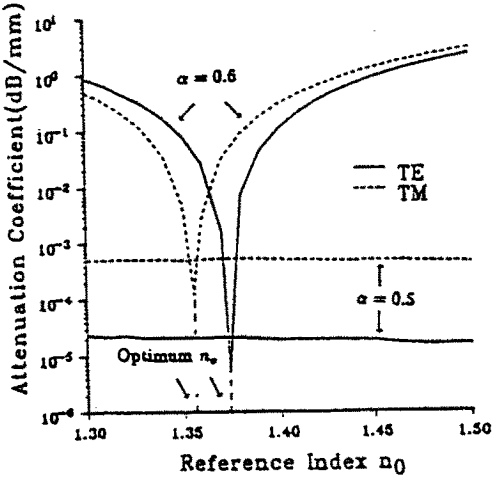

Figure 1. (a) Percentage error of propagation constant and (b) power attenuation coefficient as a function of reference index n_o.

(a)

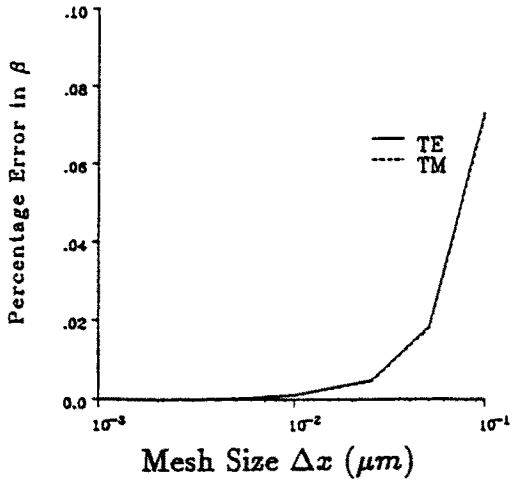

(b)

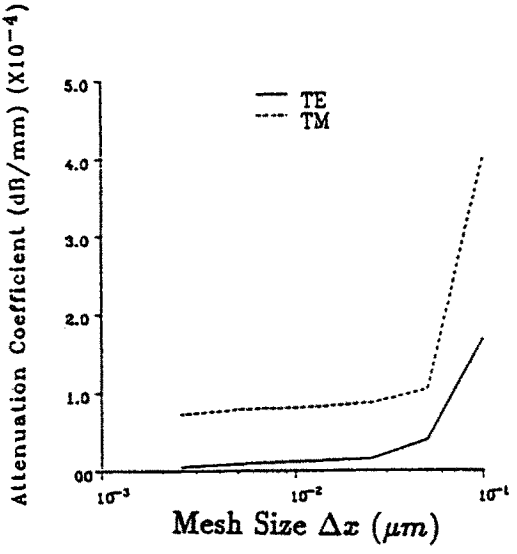

Figure 2. (a) Percentage error of propagation constant and (b) power attenuation coefficient as a function of window size.

The effect of the longitudinal step size Δz is also investigated and it is found that the variation of the longitudinal step size does not have much influence on the accuracy of the propagation constants and power attenuation coefficient [28]. In all the simulation, no instability was observed.

To investigate the effectiveness of the transparent boundary conditions, we repeated the above calculations for different window sizes. The scheme parameter $\alpha = 0.6$ is assumed and all the other parameters are the same as in Fig. 1. Figure 3(a) and 3(b) illustrate the results (solid: TE; dash: TM). It is noted that the errors in the propagation constants are virtually independent of the window sizes, indicating that the possible reflections at the edges of the computation window are negligible even for very small window size. The power attenuation coefficients increase rapidly as the window size becomes very small. This effect is to be expected: when the transparent boundary is too close to the core of the waveguide, the power that is guided in the cladding near the core region may pass through the boundary and get lost, leading to the higher attenuation. Nevertheless, the transparent boundary condition seems to be highly effective in absorbing waves traveling towards the edge of the computation window. As the window size increases, the attenuation decreases and converge to the minimum values determined by the scheme parameter α and other parameters.

The definite advantages of the present transparent boundary condition over the damping absorbing boundary condition are its accuracy, efficiency, robustness and relative independence of the waveguide structures.

B. 3-D fiber

It is expected that the conclusions for 2-D FD-BPM are still valid for 3-D FD-BPM. Since there is no polarization coupling in 2-D cases, it is necessary to verify and assess the 3-D full-vectorial FD-BPM, which takes both the polarization dependence and the polarization coupling into account. We take a step-index circular fiber as an example [37]. It is well known that the so called single mode fiber can support two fundamental vectorial modes, namely, HE_{11} modes, although both can be approximated by LP_{01} modes polarized along x and y directions by ignoring the minor field component. The indices of the core and cladding of the fiber are $n_1 = 1.469$, $n_2 = 1.460$, respectively. The radius is $a = 3.0\mu m$. The wavelength is $\lambda = 1.55\mu m$.

(a)

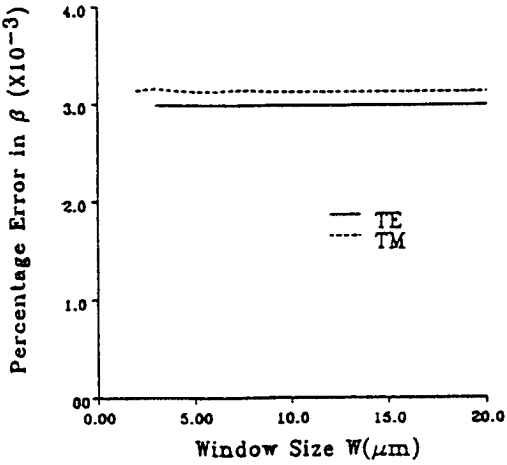

(b)

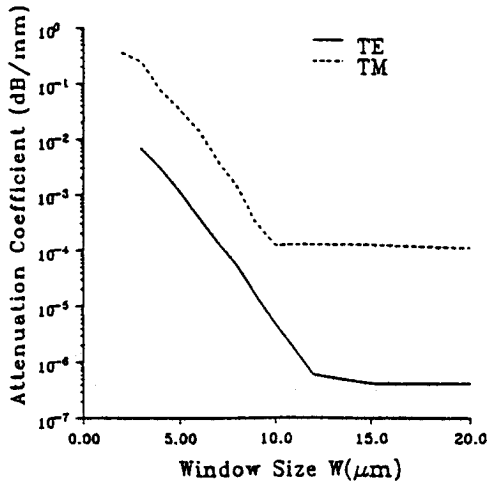

Figure 3. (a) Percentage error of propagation constant and (b) power attenuation coefficient as a function of window size.

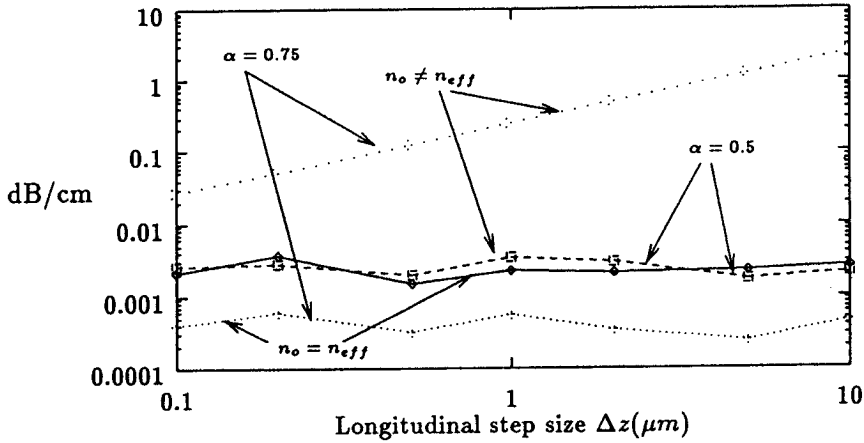

Figure 4. The numerical dissipation as a function of longitudinal step size Δz at $\Delta x = \Delta y = 0.24\mu m$

The computation window size is $W_x = W_y = 12\mu m$. The effect of longitudinal step size Δz on the stability and numerical dissipation is first investigated. The mesh sizes are $\Delta x = \Delta y = 0.24\mu m$. We compare the Crank-Nicolson scheme ($\alpha = 0.5$) with a non-Crank-Nicolson scheme ($\alpha = 0.75$). For each scheme we take two cases: $n_o = n_{\text{eff}}$ and $n_o \neq n_{\text{eff}}$, where $n_{\text{eff}} = 1.46366$ is the effective index of the HE_{11} mode of the fiber. Shown in Fig. 4 is the power attenuation coefficient as a function of longitudinal step size Δz. It is noted that the numerical dissipation of the Crank-Nicolson scheme is very small and almost independent of Δz and n_o. However, for the non-Crank-Nicolson scheme, the choice of reference index n_o is critical. If $n_o \neq n_{\text{eff}}$, the numerical dissipation is large and becomes larger as Δz increases. If $n_o = n_{\text{eff}}$, which is very difficult to obtain in practice, the numerical dissipation is very small, even smaller than the Crank-Nicolson scheme. This behavior is similar to what we observed in 2-D FD-BPM and similar explanation is valid.

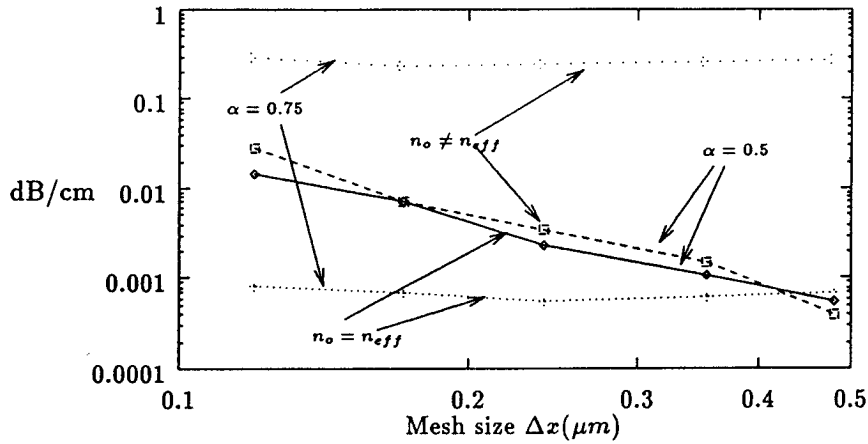

Figure 5. The numerical dissipation as a function of mesh size $\Delta x = \Delta y$ at $\Delta z = 1.0\mu m$

Also, we investigate the effect of mesh sizes Δx and Δy. The longitudinal step size is fixed at $\Delta z = 1.0\mu m$. Shown in Fig. 5 is the power attenuation as a function of mesh sizes $\Delta x = \Delta y$ for the four cases shown in Fig. 4. It is noted that the choice of n_o is very critical for the non-Crank-Nicolson scheme and has no effect on the Crank-Nicolson scheme. Also the numerical dissipation becomes larger as Δx decreases for Crank-Nicolson scheme and remains unchanged for non-Crank-Nicolson schemes. As we predicted, the FD-BPM is stable for all the simulations.

3.5 Applications

In this section, we apply the FD-BPM to two different structures. One is a 2-D grating assistant coupler and another one is a 3-D polarization rotator, for which the full-vectorial BPM has to be used since the polarization rotation is due to the coupling of the two orthogonal polarizations.

A. Grating-assisted directional coupler.

Directional couplers are building blocks for many guided-wave devices in integrated optics [45]. Typical examples of directional coupler

devices are the polarization splitters [46], wavelength filters [47], and switches or modulators [48]. In order to achieve complete power coupling between two parallel waveguides, the phase–matching condition must be satisfied, i.e., the propagation constants of the two waveguides have to be equal

$$\beta_1 = \beta_2 \tag{53}$$

Therefore, the two waveguides are either identical or carefully designed such that the propagation constants happen to be the same at the operating wavelength.

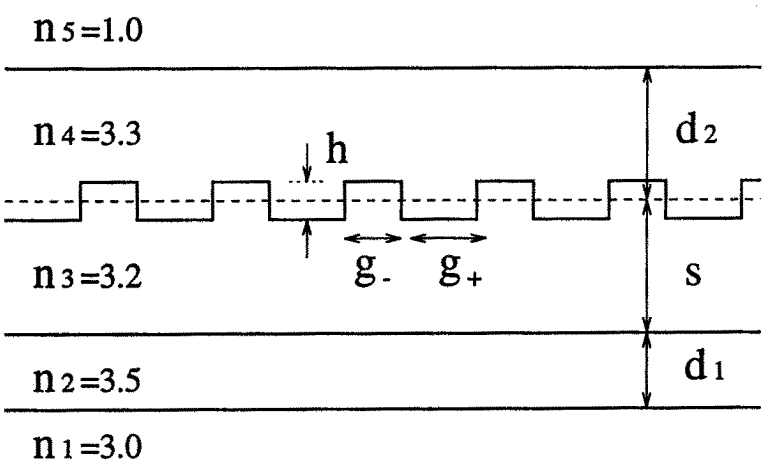

Figure 6. The schematic diagram of the grating-assisted coupler.

If the phase-matching condition (53) can not be satisfied, complete power coupling can still be achieved by introducing a proper periodic grating. Figure 6 shows the schematic diagram of a grating-assisted coupler. Two dielectric waveguides are placed in close proximity to permit coupling through the interaction of the evanescent fields of their guided modes. A grating is placed on one of the waveguides in the direction of wave propagation in order to match the phases of modes with different propagation constants, so that efficient power exchange between the two waveguides may occur. The phase-matching condition for the grating-assisted coupler is [49]

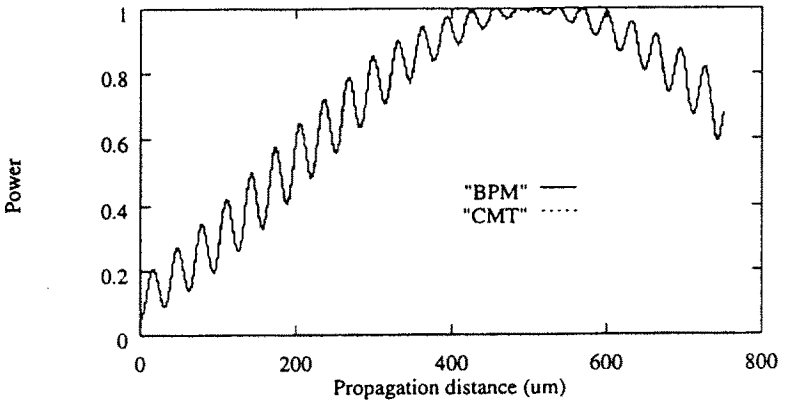

Figure 7. Power coupled to the lower waveguide of the coupler.

$$\Lambda = \frac{2\pi}{\beta_s - \beta_a} \tag{54}$$

where β_s and β_a are the propagation constants of the symmetric and antisymmetric modes of the coupler, and Λ is the grating period.

We first make a comparison with the well-established coupled-mode theory (CMT) [50]. The fundamental mode of the upper waveguide is assumed as the input field at the beginning and power will gradually couple into the lower waveguide due to the grating. Shown in Fig. 7 are the results calculated by both the FD-BPM and the CMT. The parameters used are: $d_1 = 0.3\mu m$, $d_2 = 1.0\mu m$, $s = 0.6\mu m$, $n_1 = 3.0$ $n_2 = 3.5$, $n_3 = 3.2$, $n_4 = 3.3$, $n_5 = 1.0$. It is noted that the BPM and the CMT are in excellent agreement.

An interesting result is that it makes a difference if we start the grating from a "+" section or a "–"section. Fig. 8 shows the TE mode power coupled to the lower waveguide as a function of propagation distance for these two cases. All the parameters are the same as in Fig. 7.

It is noted that the coupled power increases directly if the grating starts with a "+" section while it decreases to zero first and then increases if the grating starts with a "–" section. As a result, there is a shift which is much longer than half period. This phenomenon is consistent with the CMT results [49].

The TM case is also studied and the results are shown in Fig. 9. Similar behavior is observed.

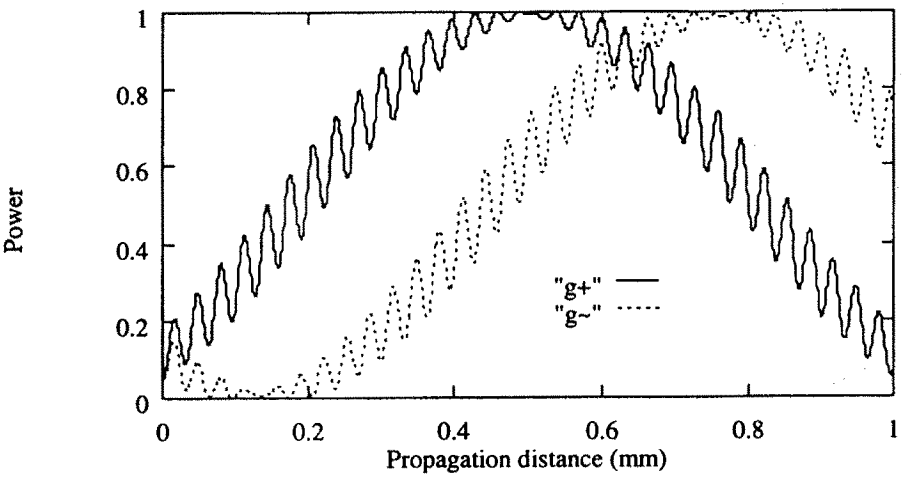

Figure 8. Power coupled to the lower waveguide by staring the coupler at different positions for TE Wave.

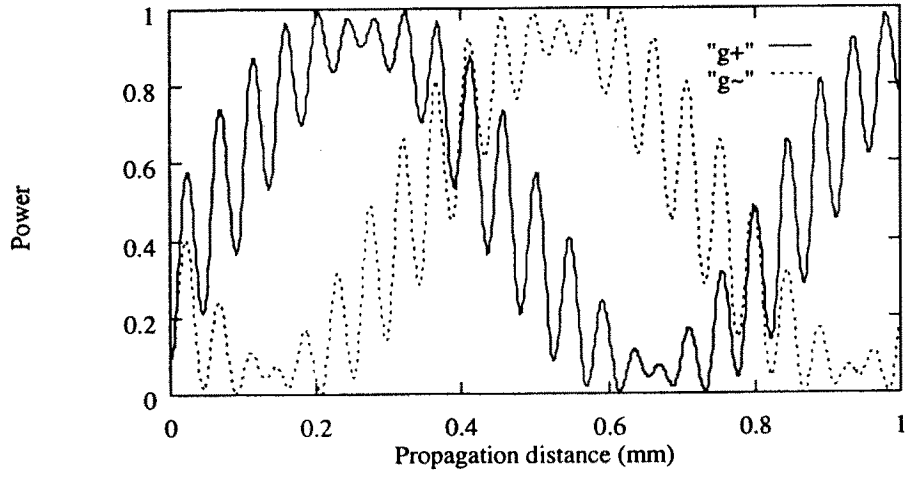

Figure 9. Power coupled to the lower waveguide by staring the coupler at different positions for TM Wave.

As we can see from above curves, the coupling process involves two different coupling mechanisms. The fast oscillation is due to the natural coupling between the two waveguides and the slowly-varying envelope is the accumulated coupling effect due to the periodic grating. Because of the nonorthogonality of the waveguide modes, a cross-talk is introduced, which causes an initial phase shift between the positions of the maximum power in one waveguide and of the minimum in the other waveguide. The power in two waveguides can be approximately written as

$$P_1 = \cos(N\phi_g) \tag{55}$$

$$P_2 = \sin(N\phi_g + \phi_0) \tag{56}$$

where ϕ_g is the phase shift introduced at each junction and N is the number of grating period. For a given structure, the initial phase angle ϕ_o (i.e., the cross-talk) and the magnitude of ϕ_g are fixed. But the sign of the ϕ_o can be positive or negative depending on whether the grating starts with a "+"or a "–" section. This makes these two cases quite different. The difference will be smaller as the separation between two waveguides becomes larger.

The scattering loss of the grating-assisted coupler may be calculated by using the FD-BPM. In this respect, the BPM is superior to the CMT, which usually treats the guided modes only. In order to precisely predict the loss, the nondissipative Crank-Nicolson scheme has to be used. Shown in Fig. 10(a) is the loss of the TE mode as a function of the propagation distance for different grating heights. It is observed that the scattering loss almost linearly depends on the grating height. It is also observed that the loss is not uniform along the propagation distance. This is reasonable considering that the radiation loss is purely due to the scattering at the junction. The loss will be minimized if all the power is guided in the waveguide without grating and no evanescent field extends to the junction.

The loss for the TM mode are also calculated and the results are shown in Fig. 10(b). Similar behaviors are observed. It is noted that the TM case is less lossy than the TE case. In addition, the TM case is more noisy than the TE case. This may be due to the discontinuities of the electric field and the nondissipative scheme ($\alpha = 0.5$).

(a)

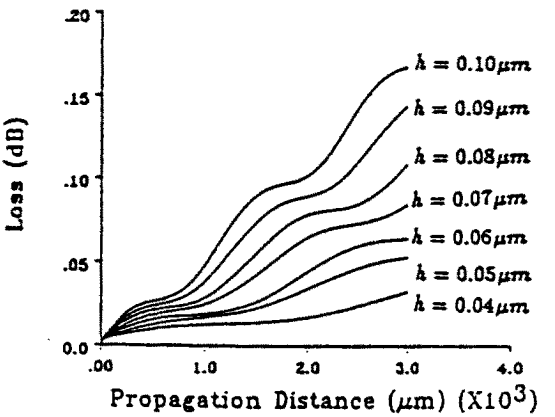

(b)

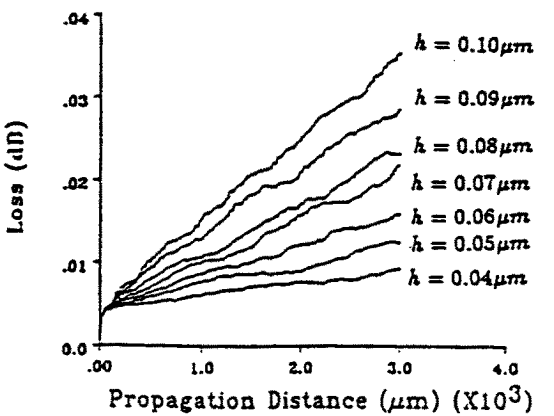

Figure 10. Radiation loss of the grating-assisted coupler as function of propagation distance for different grating heights. (a) TE wave; (b) TM wave.

B. Polarization rotator.

The polarization coupling of photonic guided-wave devices is weak due to the small index difference of the devices, hence, semi-vectorial approximation is usually sufficient. However, as the optical wavelength is very short ($0.6 - 1.6\mu m$), the weak coupling may accumulate in a relatively long device. A periodic loaded semiconductor rib waveguide is one example. Fig. 11 shows the schematic diagram of such a device. A similar structure has been fabricated and tested at AT&T Bell Labs. by Shani and coworkers [51] and a coupled-mode analysis of this device has been proposed by Huang and Mao [52]. The analysis indicates that the polarization rotation is purely due to the vectorial properties of the guided modes in the asymmetrically loaded rib waveguide. A simulation by the FD-BPM is carried out in this section. In comparison with the intuitive coupled-mode analysis, the BPM simulation is expected to be more accurate. In particular, the scattering loss at each junction can be predicted by the BPM. In the simulation, the parameters used are: the indices $n = 3.27$ for InP and $n = 3.4$ for InGaAsP, the rib width $W = 3\mu m$ and the height $H = 0.5\mu m$, the thickness of the load is $D = 0.1\mu m$, and the operating wavelength $\lambda_o = 1.3\mu m$. Two fundamental modes can be supported by this structure; one is the quasi-TE mode and the other is the quasi-TM mode. If both modes can be excited, they will propagates separately and beat with each other. As a result of the beating between these two normal modes, the two orthogonal polarizations are coupled and complete coupling can only be achieved when these two normal modes have the same amplitude. Therefore, for a straight asymmetrically loaded waveguide, complete polarization rotation cannot be achieved, since a linearly polarized input can not equally excite both modes. Figure 12 shows the power coupling between the two orthogonal polarizations when the rib waveguide is loaded asymmetrically on one-side only. It is noted that the coupling is very weak and complete polarization rotation can not be achieved. However, if we load the rib waveguide periodically and the period chosen to be the beat length as indicated in Fig. 12, complete polarization rotation can be achieved. Shown in Fig. 13 is the BPM simulation result. Figure 13(a) shows the powers carried by the two polarizations as a function of propagation distance. It is noted that an efficient polarization coupling (a complete rotation within $800\mu m$) is demonstrated. In Fig. 13(a) the results excludes the radiation loss. The results including the effect of the radiation loss is illustrated in

Fig. 13(b). It is noted that the device simulated suffers a scattering loss of about 3 dB for one coupling length. This is mainly due to the scattering at the discontinuities along the waveguide axis.

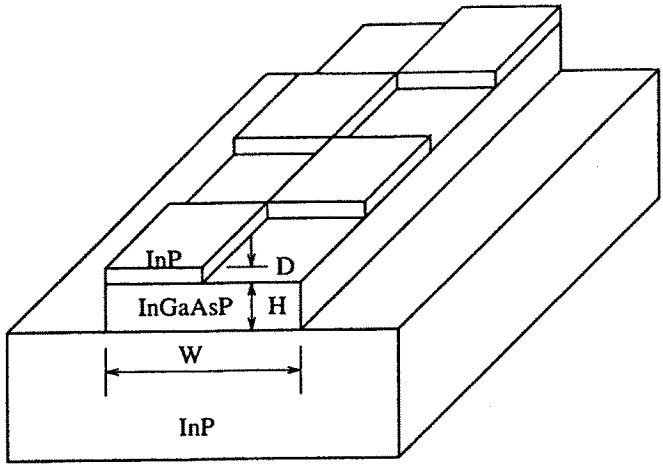

Figure 11. The schematic diagram of the periodically loaded polarization rotator.

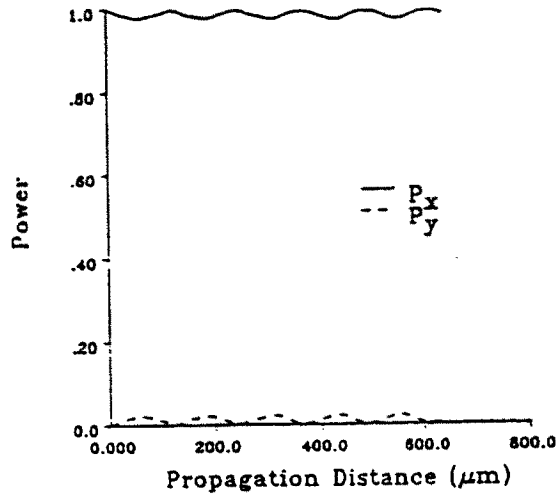

Figure 12. The power exchange between the two polarizations as a function of the propagation distance for one-side loading.

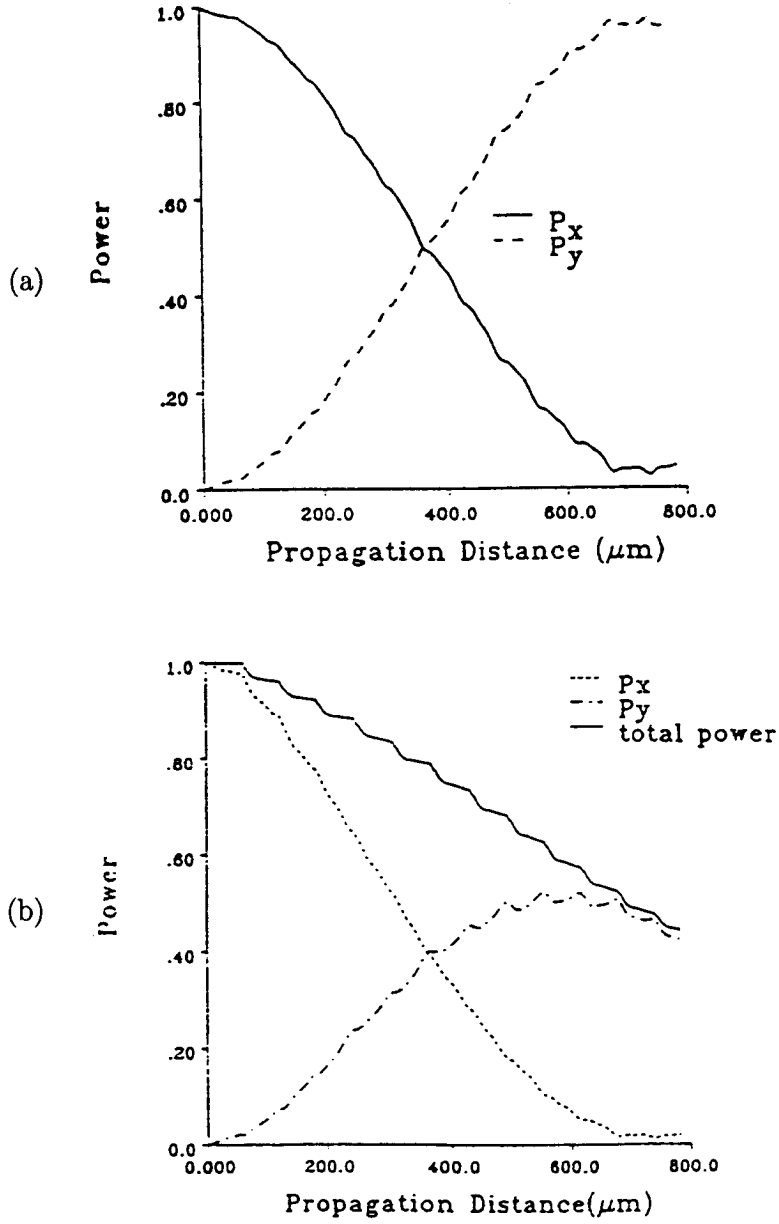

Figure 13. The power exchange between the two polarizations as a function of the propagation distance for periodic loading: (a) Scattering loss excluded; (b) Scattering loss included.

4. Other Numerical Schemes

In addition to the FD-BPM described in Section 3, there are several other numerical schemes based on finite-difference or other techniques which can be used to solve Eqs. (27) and (28) as well as their reduced semi-vectorial and scalar variants. Depending on the type of scheme employed, the propagators that relate the fields at two or more propagation steps along z may be explicit, implicit, or mixed. In this section, we focus on the following two explicit finite-difference schemes for the paraxial equations only.

4.1 Multi-Step FD-BPM

By applying a central difference to approximate the left-hand side of Eq. (27), Chung and Dagli proposed an explicit multi-step scheme [20]

$$\mathbf{E}_t(z+\Delta z) = \mathbf{E}_t(z-\Delta z) - j\frac{\Delta z}{n_o k}\mathbf{P}\mathbf{E}(z) \tag{57}$$

This scheme was originally applied to the scalar Eq. (29) and recently was extended to the vectorial equation. It is conditionally stable and a stability criterion has been derived [33] as

$$\Delta z \leq \frac{2kn_o}{\frac{4}{\Delta x^2} + \frac{4}{\Delta y^2} + k^2|n^2 - n_o^2|} \tag{58}$$

It is also demonstrated that the muti-step scheme is nondissipative, i.e., power is conserved.

One of the advantages of the multi-step FD-BPM is its simplicity in implementation; an extremely simple algorithm can be developed for the paraxial waves in both two- and three-dimensions. Since no matrix inversion is required in the propagator, this scheme is strictly explicit and particularly attractive for the three-dimension simulations, in which the solutions of the matrix equations in the implicit schemes may become difficult. At the edge of the computation window, an absorbing boundary condition (ABC) has been used and the scheme appeared to be stable. The transparent boundary condition (TBC) has not been reported for the multi-step FD-BPM. The authors have tried to use the TBC in this scheme and observed instabilities.

The stability criterion in Eq. (58) requires that the ratio between the longitudinal and the transverse step sizes be smaller than certain

value. For a fine mesh over the transverse cross-section, a very small longitudinal step size has to be used, which makes the simulation less efficient. Another difficulty reported for this scheme was that it requires the fields at *two* previous steps to predict the values of the fields at the present step. Since the field values are known only at one step, the values at the second step were calculated by using a FFT-BPM or an unstable forward-difference FD-BPM [53]. Furthermore, the use of the absorbing boundary condition (ABC) makes this scheme less robust. For instance, the scheme may become unstable due to an improper absorber.

4.2 Series-Expansion FD-BPM

By using a Taylor expansion of the exponential operators in Eq. (45), the propagator can be written as [16]

$$\mathbf{E}_t(z+\Delta z) = \sum_{n=0}^{N} \frac{1}{n!} \left(-j\frac{\Delta z \mathbf{P}}{2n_o k}\right)^n \mathbf{E}_t(z) \tag{59}$$

This scheme is explicit for the paraxial wave equation. It requires the field values at only the previous step instead of two steps in the multi-step FD-BPM. Another advantage of this scheme is that the transparent boundary condition may be applied at the edge of the computation window as demonstrated by Splett and coworkers [16]. Like the multi-step FD-BPM, the series-expansion FD-BPM was first applied to the scalar wave equation and then was extended to the vectorial wave equation [34]. One of the difficulties associated with this scheme is the stability. So far, no stability criteria have been established. In the numerical simulations, it is noted that the stability of the scheme depends on not only the step sizes, but also on the order of expansion N.

4.3 Comparisons among Different Schemes

In this section, we compare the two explicit FD-BPM schemes with the implicit scheme described in Section 3. It should be noted that it is difficult to make a direct comparison since each scheme has it own adjustable parameters, such as ABC in the multi-step scheme and the serial order in the series-expansion scheme, as well as the scheme parameter α in the implicit scheme. However, the efficiency of each scheme has nothing to do with those parameters. Therefore, we only compare the efficiency of each scheme.

For the two-dimensional structure, we choose a directional coupler which consists of two identical slab waveguides. The refractive indice are $n = 1.5$ for the core and $n = 1.3$ for the cladding. The slab waveguides are $d = 0.6\lambda$ thick with $s = 0.6\lambda$ separation. The computation window size is chosen as $w = 5\lambda$. The propagation distance is one coupling length of the coupler, i.e. $L = 49.5\lambda$. First, the mesh size (transverse step size) is fixed at $\Delta x = 0.05\lambda$ and the efficiency as a function of longitudinal step size Δz is tested. Shown in Fig. 14 are the computation times of each scheme on a HP9000/730 workstation. It is observed that the computation time is almost inversely proportional to the longitudinal step size. It is seen that the multi-step FD-BPM is the most efficient one, about one order of magnitude faster than the implicit FD-BPM for the **same** Δz. The implicit FD-BPM can be more efficient than the multi-step FD-BPM by using large step size without much sacrifice of accuracy. In contrast, the series-expansion FD-BPM appears to be the least efficient one. Also the computation time is linearly proportional to the expansion order n.

We also examined the dependence of the efficiency on the transverse step size Δx and the results are shown in Fig. 15. The longitudinal step size is fixed as $\Delta z = 0.005\lambda$. As expected, the computation time for each scheme is proportional to the number of mesh points, i.e. inversely proportional to the transverse step size Δx.

To further assess and compare the FD-BPM schemes examined, we have also simulated a three-dimensional waveguide structure. Since our focus is on the efficiency, we simply propagate the fundamental scalar mode (LP_{01}) of a step-index circular fiber for 50 wavelength. The parameters of the fiber are the index of the core: $n = 1.5$, the index of the cladding: $n = 1.48$, and the radius: $a = 2\lambda$. The computation window is $w_x = w_y = 10\lambda$. Figures 16 and 17 show the results. Similar behaviors to 2-D cases are observed. The computation time for the implicit FD-BPM is not quite linear due to the iterative sparse matrix solver. For large step size or fine mesh size, it takes more iterations to converge to a fixed tolerance.

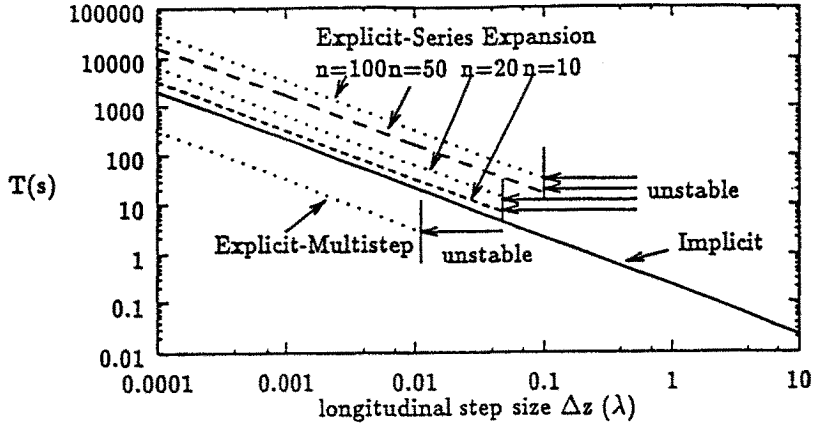

Figure 14. The computation time of different schemes as a function of longitudinal step size Δz for the 2-D structure. The transverse step size is fixed at $\Delta x = 0.05\lambda$.

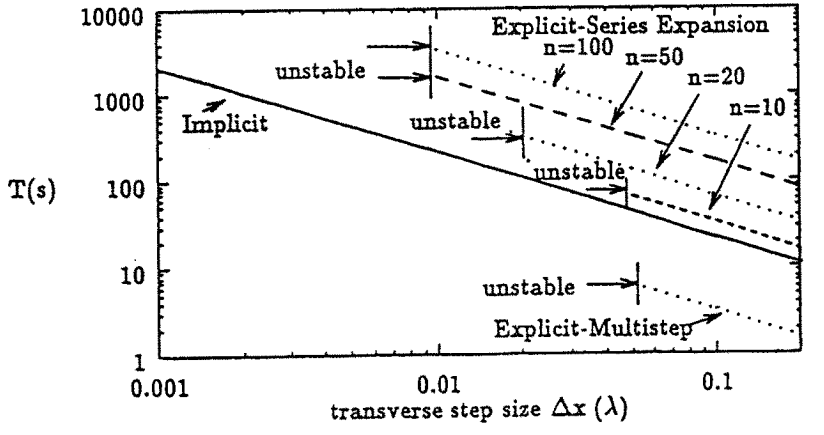

Figure 15. The computation time of different schemes as a function of transverse step size Δx for the 2-D structure. The longitudinal step size is fixed at $\Delta z = 0.005\lambda$.

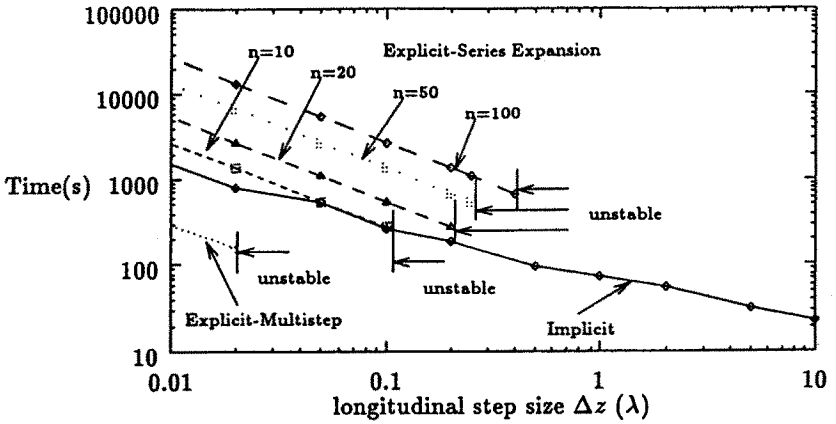

Figure 16. The computation time of different schemes as a function of longitudinal step size Δz for the 3-D structure. The transverse step size is fixed as $\Delta x = 0.1\lambda$.

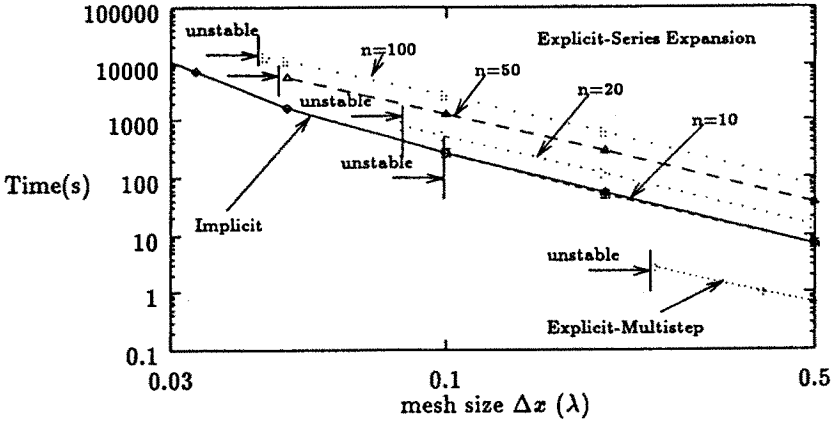

Figure 17. The computation time of different schemes as a function of transverse step size Δx for the 3-D structure. The longitudinal step size is fixed as $\Delta z = 0.1\lambda$.

In conclusion, for the **same** Δx and Δz, the multi-step explicit FD-BPM is the most efficient, and the series-expansion explicit FD-BPM is the least. However, in order to obtain more accurate results, finer meshes have to be used and the propagation step size has to be small in order to satisfy the stable condition Eq. (58), which can be approximated as

$$\frac{\Delta z}{\min[(\Delta x)^2, (\Delta y)^2]} \leq \frac{kn_o}{4} \tag{60}$$

when mesh size is very small. In this case, the multi-step scheme becomes less efficient and the implicit FD-BPM becomes more efficient due to its unconditional stability.

5. Extension the FD-BPM to Anisotropic Media

The implicit FD-BPM described in the previous sections applies to isotropic waveguides only. However, anisotropic materials are often used as guiding media for many optical devices such as polarization converters [54] and polarization maintaining fibers [55,56]. For an anisotropic medium, the propagating waves are polarization dependent and coupled due to both the material properties and the structure geometries. The BPMs have been employed for the analysis and simulation of wave propagation in anisotropic media [57–60]. The conventional BPMs, however, pertain to the scalar wave equation, where the polarization dependence and coupling due to the geometric effects are ignored. Recently, there has been some efforts in trying to bring the vectorial properties into the BPM [59,60]. However, the geometry induced polarization dependence and coupling, which is due to the discontinuities of the normal component of the electric field at discontinuous index boundaries, as well as the coupling between the longitudinal component and the transverse components of the field, are not well stated in the papers. It is not clear how the discontinuity was handled in Ref. [59] since the normal component of the electric field is not continuous and it can not be differentiated directly. In Ref. [60], the coupling between the longitudinal field and the transverse field was ignored, hence, the geometric effect was not complete.

In this section, we extend the implicit FD-BPM to waveguide structures made of anisotropic materials so that the polarization dependence and coupling due to both the material and geometric effects

can be simulated.

The equations derived in Section 2 are valid for isotropic materials only. For anisotropic media, the refractive index n^2 is replaced by a dielectric tensor $\tilde{\epsilon}$. These equations have to be modified accordingly.

5.1 Modification of Formulations

For most anisotropic materials, such as $LiNbO_3$, if the crystal axes of orientation and the applied modulation field are arranged properly, the dielectric tensor can take the form

$$\tilde{\epsilon} = \begin{pmatrix} \epsilon_{xx} & \epsilon_{xy} & 0 \\ \epsilon_{yx} & \epsilon_{yy} & 0 \\ 0 & 0 & \epsilon_{zz} \end{pmatrix}. \tag{61}$$

The variant of Eq. (14) for linear, anisotropic materials is

$$\frac{\partial^2 \mathbf{E_t}}{\partial z^2} - j2n_o k \frac{\partial \mathbf{E_t}}{\partial z} + \nabla_t^2 \mathbf{E_t} + (\tilde{\epsilon_{tt}} - n_o^2) k^2 \mathbf{E_t}$$
$$= \nabla_t \left[\nabla_t \cdot \mathbf{E_t} - \frac{1}{n_{zz}^2} \nabla_t \cdot (\tilde{\epsilon_{tt}} \mathbf{E_t}) \right], \tag{62}$$

where

$$\tilde{\epsilon_{tt}} = \begin{pmatrix} \epsilon_{xx} & \epsilon_{xy} \\ \epsilon_{yx} & \epsilon_{yy} \end{pmatrix}. \tag{63}$$

is the transverse components of the dielectric tensor.

Following the same procedure in Section 2, one is able to derive paraxial and wide-angle equations

$$j2n_o k \frac{\partial \mathbf{E_t}}{\partial z} = \mathbf{R} \mathbf{E_t} \tag{64}$$

$$j \left(2n_o k + \frac{\mathbf{R}}{2n_o k} \right) \frac{\partial \mathbf{E_t}}{\partial z} = \mathbf{R} \mathbf{E_t}. \tag{65}$$

Where the operator

$$\mathbf{R} = \begin{pmatrix} R_{xx} & R_{xy} \\ R_{yx} & R_{yy} \end{pmatrix} \tag{66}$$

is defined as [61]

$$R_{xx}E_x = \frac{\partial^2 E_x}{\partial y^2} + \frac{\partial}{\partial x}\left[\frac{1}{n_{zz}^2}\frac{\partial(n_{xx}^2 E_x)}{\partial x}\right] + \frac{\partial}{\partial x}\left[\frac{1}{n_{zz}^2}\frac{\partial(n_{yx}^2 E_x)}{\partial y}\right] + (n_{xx}^2 - n_o^2)k^2 E_x \tag{67}$$

$$R_{yy}E_y = \frac{\partial^2 E_y}{\partial x^2} + \frac{\partial}{\partial y}\left[\frac{1}{n_{zz}^2}\frac{\partial(n_{yy}^2 E_y)}{\partial y}\right] + \frac{\partial}{\partial y}\left[\frac{1}{n_{zz}^2}\frac{\partial(n_{xy}^2 E_y)}{\partial x}\right] + (n_{yy}^2 - n_o^2)k^2 E_y \tag{68}$$

$$R_{xy}E_y = n_{xy}^2 k^2 E_y + \frac{\partial}{\partial x}\left[\frac{1}{n_{zz}^2}\frac{\partial(n_{yy}^2 E_y)}{\partial y}\right] + \frac{\partial}{\partial x}\left[\frac{1}{n_{zz}^2}\frac{\partial(n_{xy}^2 E_y)}{\partial x}\right] - \frac{\partial^2 E_y}{\partial x \partial y} \tag{69}$$

$$R_{yx}E_x = n_{yx}^2 k^2 E_x + \frac{\partial}{\partial y}\left[\frac{1}{n_{zz}^2}\frac{\partial(n_{xx}^2 E_x)}{\partial x}\right] + \frac{\partial}{\partial y}\left[\frac{1}{n_{zz}^2}\frac{\partial(n_{yx}^2 E_x)}{\partial y}\right] - \frac{\partial^2 E_x}{\partial y \partial x}. \tag{70}$$

It is noted that in Eqs. (67)–(69) both the material and the geometrical properties of the waveguides contribute to the polarization dependence (i.e., $R_{xx} \neq R_{yy}$) and coupling (i.e., $R_{xy} \neq 0$ and $R_{yx} \neq 0$). If the material anisotropy and the geometric polarization effect are weak, then the "higher order" terms such as $\frac{\partial}{\partial x}\left[\frac{1}{n_{zz}^2}\frac{\partial}{\partial y}\left(n_{yx}^2 E_x\right)\right]$, $\frac{\partial}{\partial y}\left[\frac{1}{n_{zz}^2}\frac{\partial}{\partial x}\left(n_{xy}^2 E_y\right)\right]$, $\frac{\partial}{\partial x}\left[\frac{1}{n_{zz}^2}\frac{\partial}{\partial x}\left(n_{xy}^2 E_y\right)\right]$, and $\frac{\partial}{\partial y}\left[\frac{1}{n_{zz}^2}\frac{\partial}{\partial y}\left(n_{yx}^2 E_x\right)\right]$ in Eqs. (6) may be neglected. These terms, which are the "product" of the geometric and material effects, are expected to be very small for practical cases. The operators can then be approximated by

$$R_{xx}E_x = \frac{\partial^2 E_x}{\partial y^2} + \frac{\partial}{\partial x}\left[\frac{1}{n_{zz}^2}\frac{\partial(n_{xx}^2 E_x)}{\partial x}\right] + (n_{xx}^2 - n_o^2)k^2 E_x \tag{71}$$

$$R_{yy}E_y = \frac{\partial^2 E_y}{\partial x^2}E_y + \frac{\partial}{\partial y}\left[\frac{1}{n_{zz}^2}\frac{\partial(n_{yy}^2 E_y)}{\partial y}\right] + (n_{yy}^2 - n_o^2)k^2 E_y \qquad (72)$$

$$R_{xy}E_y = n_{xy}^2 k^2 E_y + \frac{\partial}{\partial x}\left[\frac{1}{n_{zz}^2}\frac{\partial(n_{yy}^2 E_y)}{\partial y}\right] - \frac{\partial^2 E_y}{\partial x \partial y} \qquad (73)$$

$$R_{yx}E_x = n_{yx}^2 k^2 E_x + \frac{\partial}{\partial y}\left[\frac{1}{n_{zz}^2}\frac{\partial(n_{xx}^2 E_x)}{\partial x}\right] - \frac{\partial^2 E_x}{\partial y \partial x} \qquad (74)$$

Similar to operators **P** for isotropic media, the discontinuities of the fields and their derivatives are considered in the formulations and the operators defined in Eqs. (71)–(74) can be discretized directly. The same numerical scheme can be used.

5.2 Example of Anisotropic Waveguides

To demonstrate the application of the FD-BPM for anisotropic waveguides, we choose a single mode step-index fiber made of birefringent materials. Due to the birefringence, the X-polarized field and the Y-polarized field see different refractive indices n_x and n_y (assuming $n_x = n_z > n_y$), respectively. Hence, two fundamental modes (X-dominant HE_{11} and Y-dominant HE_{11}) of the single mode fiber have different propagation constants. When the birefringence is sufficiently large such that the effective index of the Y-dominant HE_{11} mode is smaller than the cladding index n_x^{clad}, the Y-dominant HE_{11} will coupled to the X-polarized radiation mode, which has a continuous spectrum. Therefore, a single polarized, single mode fiber can be realized. The coupling loss has been studied by using both perturbation theory [62] and coupled-mode theory [63]. A closed form analytical solution has been derived [62]. To verify the phenomenon and make a comparison, we use the BPM to calculate the loss of a single mode birefringent fiber. The radius of the fiber is $R = 5\mu m$ and the wavelength is $\lambda = 1.55\mu m$. The refractive indices of the core and cladding are $n_x^{co} = 1.4646$ and $n_x^{clad} = 1.46$ in X-direction, and $n_y^{co} = n_x^{co} + \delta_{xy}$ and $n_y^{clad} = n_x^{clad} + \delta_{xy}$ in Y-direction, where δ_{xy} is the material birefringence. The HE_{11} mode of an isotropic fiber with $\delta_{xy} = 0$ is chosen as the input field and propagates in the birefringent fiber. After the steady state is reached, the loss per unit length can be calculated. Shown in Fig. 18. is the loss as a function of δ_{xy}/Δ, where $\Delta = n^{co} - n^{clad}$ is the index difference between core and cladding.

The analytical result by Ref. [62] is also shown in the same chart. It is noted that analytical result and numerical result are in very good agreement. The loss calculated by BPM is slightly larger than the analytical solution. That is due to the inevitable numerical dissipation of the BPM.

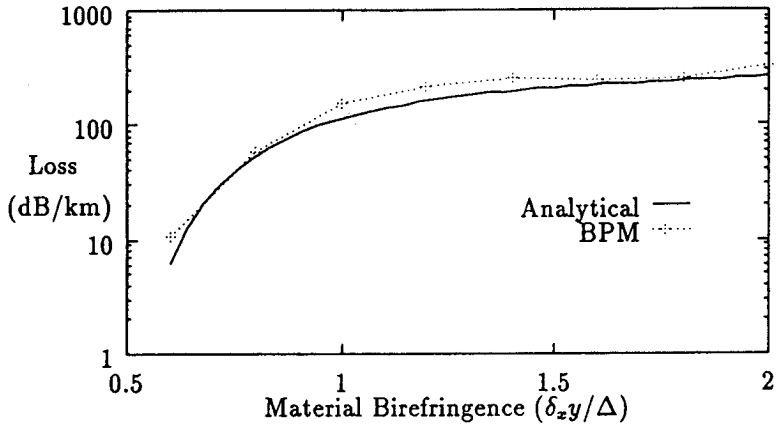

Figure 18. Loss of the Y-dominant HE_{11} mode of the birefringent fiber as a function of material birefringence.

In order to demonstrate the lossy phenomenon clearly, we plot, in Fig. 19, the field patterns of two components at the steady state. It is noted the main component is similar to the main component of an isotropic fiber. The minor component, however, is quite different from the minor component of an isotropic fiber. It is not well confined and the leakage is clearly illustrated. This phenomenon is consistent with what is predicted by perturbation theory [62]. The main component consists of guided and radiative fields. The radiation is very small compared with the guided field, hence, the leakage is hardly visible in Fig. 19. Whereas, the minor component consists of the radiative field only, hence the leakage can be clearly observed. In comparison, we also plot, in Fig. 20, the field patterns of X-dominant HE_{11} mode at the steady state. They are similar to those of an isotropic fiber and no obvious leakage is observed.

(a)

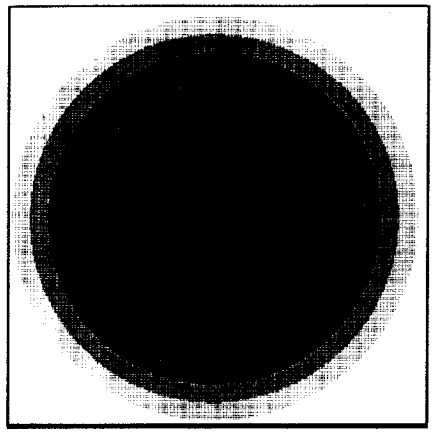

(b)

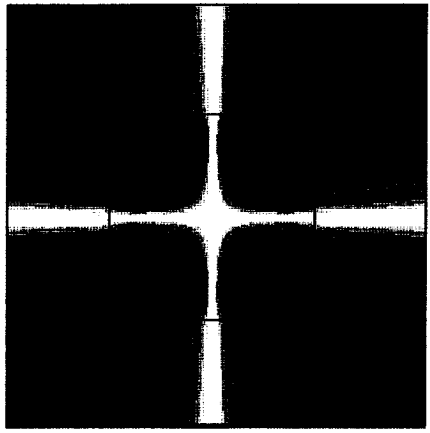

Figure 19. Field patterns of the Y-dominant HE_{11} mode of the birefringent fiber ($\delta_{xy} = \Delta$). (a) Dominated E_y component; (b) Minor E_x component.

(a)

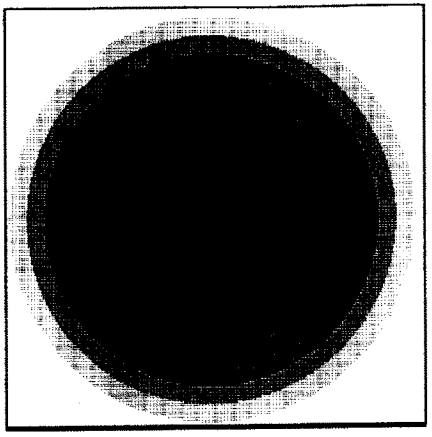

(b)

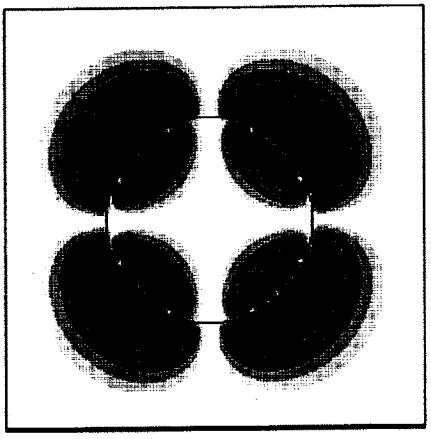

Figure 20. Field patterns of the X-dominant HE_{11} mode of the birefringent fiber ($\delta_{xy} = \Delta$). (a) Dominated E_x component; (b) Minor E_y component.

References

1. Feit, M. D., and J. A. Fleck, Jr., "Light propagation in graded-index optical fibers," *Appl. Opt.*, Vol. 17, No. 24, 3990–3998, 1978.
2. Feit, M. D., and J. A. Fleck, Jr., "Computation of mode properties in optical fiber waveguides by a propagating beam method," *Appl. Opt.*, Vol. 19, No. 7, 1154–1164, 1980.
3. Feit, M. D., and J. A. Fleck, Jr., "Computation of mode eigenfunctions in graded-index optical fibers by the propagation beam method," *Appl. Optics*, Vol. 19, No. 13, 2240–2246, 1980.
4. Baets, R., and P. E. Lagasse, "Calculation of radiation loss in integrated-optic tapers and Y-junction," *Appl. Opt.*, Vol. 21, No. 11, 1972–1978, 1981.
5. Hermansson, B., D. Yevick, and P. Danielsen, "Propagating beam analysis of multimode waveguide tapers," *IEEE J. Quantum Electron.*, Vol. 19, No. 8, 1246–1251, 1983.
6. Baets, R., and P. E. Lagasse, "Loss calculation and design of arbitrarily cured integrated-optic waveguide," *J. Opt. Soc. Am.*, Vol. 73, No. 2, 177–182, 1983.
7. Yevick, D., and L. Thylen, "Analysis of gratings by the beam-propagation method," *J. Opt. Soc. Am.*, Vol. 72, No. 8, 1084–1089, 1982.
8. Neyer, A., W. Mevenkamp, L. Thylen, and B. Lagerstrom, "A beam propagation method analysis of active and passive waveguide crossings," *IEEE/OSA J. Lightwave Tech.*, Vol. 3, No. 3, 635–642, 1985.
9. Danielsen, P., "Two-dimensional propagating beam analysis of an electrooptic waveguide modulator," *IEEE J. Quantum Electron.*, Vol. 20, No. 9, 1093–1097, 1984.
10. Kaczmarski, P., P. Lagasse, and J. Vandewege, "Propagating-beam model for a single-mode fiber fused coupler," *IEE Proc.*, Vol. 134, Pt. J, No. 2, 111–116, 1987.
11. Lamouroux, B., and B. Prade, "Three-dimensional beam-propagation method treatment of a monomode optical-fiber half-coupler," *J. Opt. Soc. Am. A*, Vol. 4, No. 12, 2228–2232, 1987.
12. Thylen, L., E. M. Wrightm, G. I. Stegeman, C. T. Seaton, and J. V. Moloney, "Beam-propagation method analysis of a nonlinear directional coupler," *Opt. Lett.*, Vol. 11, No. 11, 739–741, 1986.

13. Lagasse, P. E., and R. Baets, "Application of propagating beam methods to electromagnetic and acoustic wave propagation problems: a review," *Radio Sci.*, Vol. 22, No. 7, 1225–1233, 1987.
14. Rolland, C., G. Mak, K. Fox, D. Adams, A. Thorpe, D. Yevick, and B. Hermansson, "Analysis of strongly-guiding rib waveguide S-bends: theory and experiment," *Electron. Lett.*, Vol. 25, 1256–1257, 1989.
15. Yevick, D., and M. Glasner, "Forward wide-angle light propagation in semiconductor rib waveguide and integrated optic structures," *Electron. Lett.*, Vol. 25, 1611–613, 1989.
16. Splett, A., M. Majd, and K. Petermann, "A novel beam propagation method for large refractive index steps and large propagation distances," *IEEE Photo. Tech Lett.*, Vol. 3, No. 5, 466–468, 1991.
17. Yevick, D., and B. Hermansson, "Split-step finite-difference analysis of rib waveguides," *Electron. Lett.*, Vol. 25, 461–463, 1989.
18. Yevick, D., and B. Hermansson, "Efficient beam propagation techniques," *IEEE J. Quantum Electron.*, Vol. 26, No. 1, 109–112, 1990.
19. Hendow, S. T., and S. A. Shakir, "Recursive numerical solution for nonlinear wave propagation in fibers and cylindrically symmetric systems," *Appl. Opt.*, Vol. 25, No. 11, 1759–1764, 1986.
20. Chung, Y., and N. Dagli, "An Assessment of finite difference beam propagation method," *IEEE J. Quantum Electron.*, Vol. 26, No. 8, 1135–1139, 1990.
21. Scarmozzino, R., and R. M. Osgood Jr., "Comparison of finite-difference and Fourier-transform solutions of the parabolic wave equation with emphasis on integrated-optics applications," *J. Opt. Soc. Am. A*, Vol. 8, No. 5, 724–731, 1991.
22. Yevick, D., J. Yu, M. Munowitz, and D. Vezzetti, "Modal analyses of semiconductor rib waveguides employing nonequidistant grids," *J. Opt. Soc. Am. A*, Vol. 8, No. 9, 1385–1388, 1991.
23. Artiglia, M., P. D. Vita, M. Potenza, G. Coppa, G. Lapenta, and P. Ravetto, "Variable grid finite difference methods for study of longitudinally varying planar waveguides," *Electron. Lett.*, Vol. 27, 474–475, 1991.
24. Kim, C. M., and R. V. Ramaswamy, "Modeling of graded-index channel waveguides using nonuniform finite difference method," *IEEE/OSA J. Lightwave Tech.*, Vol. 7, No. 14, 1581–1589, 1989.

25. Seki, S., T. Yamanaka, and K. Yokoyama, "Two-dimensional analysis of optical waveguides with a nonuniform finite-difference method," *IEE Proc.*, Vol. 138, Pt. J, No. 2, 123–127, 1991.
26. Schmidt, F., and H. -P. Nolting, "Adaptive multilevel beam propagation method," *IEEE Photon. Tech. Lett.*, Vol. 4, No. 12, 1381–1383, 1992.
27. Huang, W. P., C. L. Xu, S. T. Chu, and S. K. Chaudhuri, "A vector beam propagation method for guided-wave optics," *IEEE Photon. Tech. Lett.*, Vol. 3, No. 10, 910–913, 1991.
28. Huang, W. P., C. L. Xu, S. T. Chu, and S. K. Chaudhuri, "A finite difference vector beam propagation method: analysis and assessment," *IEEE/OSA J. Lightwave Technol.*, Vol. 10, No. 3, 295–305, 1992.
29. Liu, P. -L., and B. -J. Li, "Study of form birefringence in waveguide devices using the semivectorial beam propagation method," *IEEE Photon. Tech. Lett.*, Vol. 3, No. 10, 913–915, 1991.
30. Liu, P. -L., and B. -J. Li, "Semivectorial beam-propagation method for analyzing polarized modes of rib waveguides," *IEEE J. Quantum Electron.*, Vol. 28, No. 4, 778–782, 1992.
31. Huang, W. P., C. L. Xu, and S. K. Chaudhuri, "A vector beam propagation method based on H-fields," *IEEE Photon. Tech. Lett.*, Vol. 3, No. 12, 1117–1120, 1991.
32. Huang, W. P., C. L. Xu, and S. K. Chaudhuri, "A finite-difference vector beam propagation method for three-dimensional waveguide structures," *IEEE Photon. Tech. Lett.*, Vol. 4, No. 2, 148–151, 1992.
33. Chung, Y., N. Dagli, and L. Thylen, "Explicit finite difference vectorial beam propagation method," *Electron. Lett.*, Vol. 27, 2119–2121, 1991.
34. Bothe, Splett, Unlenderf, and Pertermann, "Series-expansion-beam-propagation-method for the vector wave equation," *IPR'93* , paper WE5-1, Palm Spring, California, 1993
35. Chung, Y., N. Dagli, and L. Thylen, "An explicit finite difference wide angle beam propagation method," *IPR'93* , paper ITuI4, Palm Spring, California, 1993
36. Huang, W. P., C. L. Xu, and S. K. Chaudhuri, "A wide angle vector beam propagation method," *IEEE Photon. Tech. Lett.*, Vol. 4, No. 10, 1118–1120, 1992.

37. Xu, C. L., W. P. Huang, S. K. Chaudhuri, and J. Chrostowski, "A unconditionally stable vectorial beam propagation method," *IEEE Photon. Tech. Lett.*, to be published in April, 1994.
38. Hadley, G. R., "Wide-angle beam propagation with a transparent boundary condition," *IPR'92*, New Orleans, paper WE3-1, 1992.
39. Hadley, G. R., "Wide-angle beam propagation using Pade approximation operators," *Opt. Lett.*, Vol. 17, No. 20, 1426–1428, 1992.
40. Press, W. H., B. P. Flannery, S. A. Teckolsky, and W. T. Vetterling, *Numerical Recipes*, New York, Cambridge, 1986.
41. Behie, A., and P. K. W. Vinsome, "Block iterative methods for fully implicit reservoir simulation," *Soc. Pet. Eng. J.*, No. 10, 658–668, 1982.
42. Van Der Vorst, H. A., "Bi-CGSTAB: a fast and smoothly converging variant of Bi-CG for the solution of nonsymmetric linear system," *SIAM J. Sci. Statist. Comput.*, Vol. 13, 631–644, 1992.
43. Van Der Vorst, H. A., "Bi-CGSTAB: a fast and smoothly converging variant of Bi-CG for the solution of nonsymmetric linear system," *SIAM J. Sci. Statist. Comput.* Vol. 13, 631–644, 1992.
44. Hadley, R. G., "Transparent boundary condition for beam propagation methods," *Opt. Lett.*, Vol. 16, No. 9, 624–626, 1991.
45. Tamir, T., Ed., *Guide-Wave Optoelectronics,* New York, Springer Ser., 1988.
46. Mikami, O., "$LiNbO_3$ coupled-waveguided TE/TM mode splitter," *Appl. Phys. Lett.*, Vol. 36, 491–493, 1980.
47. Alferness, R. C., and R. V. Schmidt, "Tunable optical waveguide directional coupler filter," *Appl. Phys. Lett.*, Vol. 33, 161–163, 1978.
48. Schmidt, R. V., and R. C. Alferness, "Directional coupler switches, modulators, and filters using alternating $\Delta\beta$ techniques," *IEEE Trans. Circuits Syst.*, Vol. 26, 1099–1108, 1979.
49. Hong, J., "Modeling of passive and active grating-coupled guided-wave devices," Ph.D. thesis, University of Waterloo, 1994
50. Huang, W. P., B. Little, and C. L. Xu, "On phase matching and power coupling in grating-assisted couplers," *IEEE Photon. Tech. Lett.*, Vol. 4, No. 2, 151–153, 1992.

51. Shani, Y., R. Alferness, T. Kock, U. Koren, M. Oron, B. I. Miller, and M. G. Young, "Polarization rotation in asymmetric periodic loaded rib waveguides," *Appl. Phys. Lett.*, Vol. 59, No. 11, 1278–1280, 1991.
52. Huang, W. P., and Z. M. Mao, "Polarization rotation in periodic loaded rib waveguides," *IEEE J. Lightwave Technol.*, Vol. 10, No. 12, 1825–1831, 1992.
53. Chung, Y., and N. Dagli, "Analysis of z-invariant and z-variant semiconductor rib waveguides by explicit finite difference beam propagation method with nonuniform mesh configuration," *IEEE J. Quantum Electron.*, Vol. 27, No. 10, 2296–2305, 1991.
54. Alferness, R. C., "Efficient waveguide electro-optic TE $\rightleftharpoons$ TM mode converter/waveguide filter," *Appl. Phys. Lett.*, Vol. 36, 513–515, 1980.
55. Stolen, R. H., V. Ramaswamy, P. Kaiser, and W. Pleibel, "Linear polarization in birefringent single-mode fibers," *Appl. Phys. Lett.*, Vol. 33, 699–701, 1978.
56. Payne, D. N., A. J. Barlow, and J. J. Hansen, "Development of low- and high-birefringence fibers," *IEEE J. Quantum Electron.*, Vol. 18, No. 4, 477–487, 1982.
57. Thylen, T., and D. Yevick, "Beam propagation method in anisotropic media," *Appl. Opt.*, Vol. 21, No. 15, 2751–2754, 1982.
58. Fleck, J. A. Jr., and M. D. Feit, "Beam Propagation in uniaxial anisotropic media," *J. Opt. Soc. Am.*, Vol. 73, No. 7, 920–926, 1983.
59. Liu, J. M., and L. Gomelsky, "Vectorial beam propagation method," *J. Opt. Soc. Am. A*, Vol. 9, No. 9, 1574–1585, 1992.
60. Martin, O. J. F., R. Clauberg, and F. -K. Reinhart, "Three-dimensional vectorial beam propagation method for anisotropic medium", *IPR'93*, paper ITuI7, Palm Springs, California, 1993.
61. Xu, C. L., W. P. Huang, J. Chrostowski, and S. K. Chaudhuri, "A full-vectorial beam propagation methods for anisotropic waveguides," *IEEE J. Lightwave Tech.*, submitted in January, 1994.
62. Snyder, A. W., and F. Rühl, "Single-mode, single-polarization fibers made of birefringent material," *J. Opt. Soc. Am.*, Vol. 73, No. 9, 1165–1174, 1983.
63. Cancellieri, G., P. Fantini, and M. Tilio, "Single-mode, single-polarization fibers: effects of a residual polarization coupling," *J. Opt. Soc. Am. A*, Vol. 2, No. 11, 1885–1890, 1985.